

Review

Open Access



# Recent progress in single atomic catalysts for electrochemical N<sub>2</sub> fixation

Binbin Fan, Weijia Wang, Zhihao Liu, Jifan Guo, Hua Yuan, Ye qiang Tan

State Key Laboratory of Bio-Fibers and Eco-Textiles, School of Materials Science and Engineering, Qingdao University, Qingdao 266071, Shandong, China.

**Correspondence to:** Prof. Hua Yuan, Prof. Ye qiang Tan, State Key Laboratory of Bio-Fibers and Eco-Textiles & Institute of Marine Biobased Materials & Collage of Materials Science and Engineering, Qingdao University, 308 Ningxia Road, Qingdao 266071, China. E-mail: yuanhua@qdu.edu.cn; tanyeqiang@qdu.edu.cn

**How to cite this article:** Fan B, Wang W, Liu Z, Guo J, Yuan H, Tan Y. Recent progress in single atomic catalysts for electrochemical N<sub>2</sub> fixation. *Microstructures* 2024;4:2024025. <https://dx.doi.org/10.20517/microstructures.2023.71>

**Received:** 6 Nov 2023 **First Decision:** 12 Dec 2023 **Revised:** 26 Dec 2023 **Accepted:** 19 Jan 2024 **Published:** 30 Apr 2024

**Academic Editor:** Chunqiang Zhuang **Copy Editor:** Pei-Yun Wang **Production Editor:** Pei-Yun Wang

## Abstract

Ammonia (NH<sub>3</sub>), as an important chemical product, is industrially produced using the traditional energy-intensive Haber-Bosch method at high temperature and pressure. Electrochemical nitrogen reduction reaction (NRR) to synthesize NH<sub>3</sub> at ambient conditions has been considered as a promising candidate for replacing Haber-Bosch process. However, major obstacles, such as poor catalytic activity and selectivity and extensive competitive hydrogen evolution reaction, remain in NRR, which urgently need to be addressed. Single atom electrocatalysts (SACs) have attracted wide attention in view of their nearly 100% atomic utilization and outstanding catalytic performance. In this review, recent theoretical and experimental advances on novel atomically dispersed electrocatalysts for NRR are summarized and highlighted. We start with the fundamental reaction mechanism of NRR. Then, different preparation methods and the strategies of boosting catalytic performance of SACs from the aspects of coordination environment, coordination number, metal-support interaction and spatial microenvironment regulation are presented and analyzed in detail. Following this, the extensive applications of SACs in terms of noble metal based-SACs and transition metal-based SACs in NRR are discussed. Finally, we provide a perspective of the challenges of SACs for NRR, aiming to guide the rational design of advanced NRR catalysts.

**Keywords:** SACs, NRR, ammonia synthesis



© The Author(s) 2024. **Open Access** This article is licensed under a Creative Commons Attribution 4.0 International License (<https://creativecommons.org/licenses/by/4.0/>), which permits unrestricted use, sharing, adaptation, distribution and reproduction in any medium or format, for any purpose, even commercially, as long as you give appropriate credit to the original author(s) and the source, provide a link to the Creative Commons license, and indicate if changes were made.



## INTRODUCTION

Ammonia (NH<sub>3</sub>), as one of the most important chemical products, is widely used not only in the manufacture of fertilizers and biomedicines but also as the green energy carrier and an alternative fuel<sup>[1-3]</sup>. Up to now, the synthesis of industrial ammonia has mainly depended on the Haber-Bosch process, which is proceeding at high temperatures (300-500 °C) and high pressure (150-200 atm) with iron-based catalysts. However, this process requires high energy consumption and releases large amounts of CO<sub>2</sub> gases (accounting for 1% of the world CO<sub>2</sub> emission). For the sustainable development of energy and the environment, a green and economical process for the synthesis of NH<sub>3</sub> is essential to replace the Haber-Bosch method.

Various strategies to synthesize ammonia under mild conditions have been developed in recent years, including photocatalytic nitrogen (N) fixation, electrocatalytic nitrogen fixation [nitrogen reduction reaction (NRR)] and biochemical catalytic nitrogen fixation. Among them, NRR has great potential to efficiently produce NH<sub>3</sub> utilizing H<sub>2</sub>O as the hydrogen resource and renewable energies as the power sources. In addition, the electrochemical NRR process is able to simplify the reactor design without the employment of large equipment, thereby reducing the energy consumption during the transportation. In spite of the above advantages, the practical application of NRR is still hindered by its poor NH<sub>3</sub> yield and Faradic efficiency (FE). Firstly, the breakage and activation of inert N≡N bond (960 kJ·mol<sup>-1</sup>) at ambient conditions is difficult<sup>[4]</sup>. Secondly, the competitive hydrogen evolution reaction (HER) always occurs preferentially in aqueous solution due to the smaller theoretical limiting potential of HER than that of NRR, which will cause the reducing of FE<sup>[5]</sup>. Therefore, the electrochemical system for NRR, such as electrocatalysts, electrolytes, and electrolytic cells, should be optimized to realize high NH<sub>3</sub> yield and FE. As a key component, an advanced electrocatalyst with superior catalytic activity and high selectivity is essential to realize an efficient NRR process at ambient conditions.

It is well established that the homogeneous electrocatalytic process usually occurs on the surface of catalysts, making the limited active sites restricted to the surface of several atomic layers. Decreasing the size of catalysts to clusters or even single atoms can maximize the atomic utilization and thus greatly elevate the electrocatalytic performance<sup>[6]</sup> [Figure 1]. In 2011, Qiao *et al.* first reported the catalysts with individual Fe atomic species stabilized on the surface of iron oxides, which displayed excellent catalytic activity for CO oxidation<sup>[7]</sup>. Since then, the single atom catalysts (SACs) have attracted enormous attention and have been developed rapidly in the field of catalysis. Generally, the SACs have the following merits: (i) 100% atomic utilization and low-coordination environment make the SACs exhibit remarkable catalytic activity and selectivity toward diverse reactions; (ii) The strong force between metal active sites and support materials makes sure the atomical dispersion and stabilization of metal atoms<sup>[8]</sup>; (iii) The individual metal species enable the similar electronic structures and geometric configurations, which provide the opportunities to demonstrate the catalytic mechanism on the atomic level<sup>[9]</sup>.

In this review, we aim to provide an overview of the recent progress on the breakthroughs of the SACs. First, we demonstrate in detail the recently developed synthetic strategies to prepare SACs. Second, the effective strategies of catalytic activity enhancement for SACs in terms of coordination atoms, coordination number, metal-support interaction, and spatial microenvironment have been discussed to realize the precise design and preparation of SACs from the theoretical guidance. Third, we will summarize the breakthroughs that notable SACs have brought in NRR, including noble-metal SACs and nonnoble-metal SACs (Fe-based SACs, Mo-based SACs, and other metal-based metals). In addition, we discuss the challenges and perspectives for developing advanced SACs with desired catalytic performance toward NRR from the design principle.

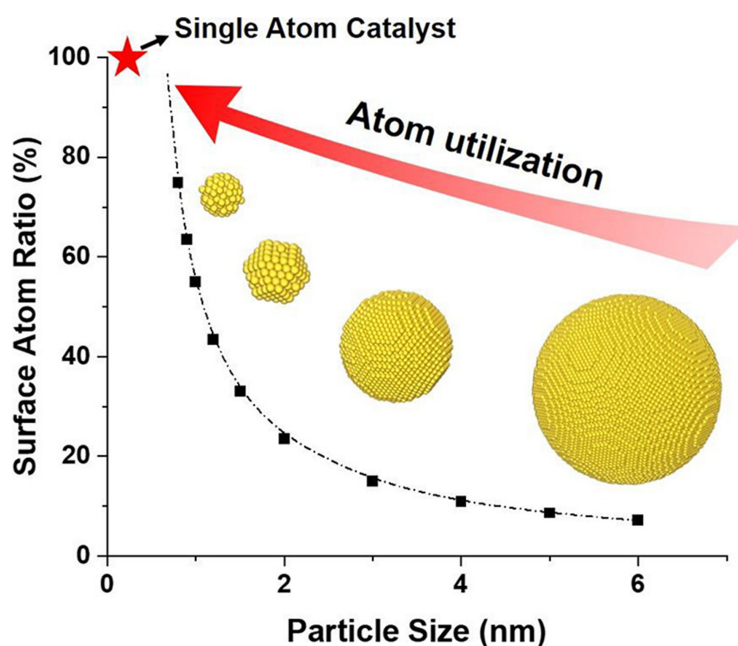


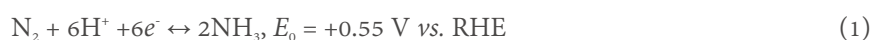
Figure 1. The surface atom ratios at different particle sizes<sup>[6]</sup>. Copyright 2023, ACS Publications.

## FUNDAMENTAL PRINCIPLES OF ELECTROCATALYTIC NRR

### Fundamentals of NRR

In the NRR process, the first bottleneck is the dissolution of  $N_2$  into an electrolyte in view of the inertness of  $N_2$  molecules, which results from the high binding energy ( $941 \text{ kJ}\cdot\text{mol}^{-1}$ ) of  $N\equiv N$  bond and lack of dipole. The second process is the adsorption of  $N_2$  molecules on the active sites and subsequent activation of  $N_2$ , accompanied by accepting electrons from electrocatalysts. Thanks to the abundant empty  $d$  orbitals in the transition metals, they can receive the lone-pair electrons of  $N_2$  and then donate electrons into the antibonding orbitals of  $N_2$ , thus activating  $N_2$  molecules. The above procedures are hindered by the adsorption of hydrogen protons in the electrolyte, which are more active than inert  $N_2$  molecules. The subsequent hydrogenation process is considered as the most difficult step due to the fact that the hydrogenation of  $N_2$  is a thermodynamic endothermic reaction ( $\Delta H = +37.6 \text{ kJ}\cdot\text{mol}^{-1}$ ).

Furthermore, the severe competing HER process is an obstacle that cannot be ignored for NRR. The readily adsorption of hydrogen protons on the active sites with low energy hinders the NRR procedure at a large extent. Although the equilibrium potentials of NRR are close to HER at not only acid [Equations (1) and (2)] but also alkaline conditions [Equations (3) and (4)], the multi-proton/electron transfer mechanism for NRR largely hinders the reaction kinetics. Consequently, a majority of protons/electrons participate in the HER process. Much more negative equilibrium potential to form  $N_2H$  verifies the difficulty of the first hydrogenation process. In contrast, the smaller redox potentials for the two-electron, four-electron, and six-electron reactions indicate that the subsequent hydrogenation steps are easier than the first-H addition process [Equations (5)-(8)].





### Reaction pathways of NRR

The NRR process mainly occurs at mild conditions with  $\text{H}_2\text{O}$  and  $\text{N}_2$  as proton and nitrogen sources, respectively [Figure 2A and B]<sup>[10,11]</sup>. Generally, the NRR process over heterogeneous catalysts is divided into two reaction pathways, including dissociative and associative pathways<sup>[12]</sup>. For a dissociative mechanism, breakage of  $\text{N}_2$  molecules first occurs, leaving isolated nitrogen atoms on the surface of catalysts. Subsequently, the nitrogen atoms are successively hydrogenated to convert into  $\text{NH}_3$  [Figure 2C]. Due to the extreme stability of  $\text{N}_2$  molecules, the dissociative reaction pathway mainly occurred in the Haber-Bosch process, requiring huge energy consumption<sup>[13,14]</sup>. Different from a dissociative pathway, two N atoms strongly joined together before the first  $\text{NH}_3$  molecule was released in the associative mechanism. Considering different sequences of a hydrogenation process, an associative reaction pathway is further separated into a distal pathway and an alternating pathway. In the distal pathway, the distal N atom preferentially undergoes the hydrogenation process for the formation of  $^*\text{NNH}$  and  $^*\text{NNH}_2$  intermediates successively until releasing the first  $\text{NH}_3$  molecule, and then, the same procedure happens on another N atom to form the second  $\text{NH}_3$  molecule [Figure 2D]. In contrast, for an alternating mechanism, two N atoms were alternatively protonated to form  $^*\text{NHNH}$  and  $^*\text{NH}_2\text{NH}_2$  intermediates and release two  $\text{NH}_3$  molecules finally [Figure 2E]. Therefore, hydrazine ( $\text{N}_2\text{H}_4$ ), as a by-product, may be generated in the alternating pathway. Moreover, the enzymatic mechanism displays a similar reaction process with an alternating mechanism except that  $\text{N}_2$  molecules are adsorbed on the electrocatalyst with a side-on configuration<sup>[15]</sup>.

Recently, an emerging Mars-van Krevelen (MvK) mechanism has also been introduced for the transition metal nitrides (TMNs) (e.g., VN, ZrN, and NbN). Unlike above-mentioned mechanisms, the surface lattice N atoms of TMNs were hydrogenated to obtain the first  $\text{NH}_3$  molecule, generating N vacancies. Then, these N vacancies were supplemented by  $\text{N}_2$  molecules in the electrolyte and resulted in the formation of the second  $\text{NH}_3$  molecule, accompanied by the decrease of lattice N atoms. Compared to the dissociative and associative mechanisms, smaller equilibrium potential is required on the  $\text{N}_2$  activation procedure in the MvK mechanism, resulting in a more beneficial NRR process.

### Catalytic activity descriptors of NRR

The FE and  $\text{NH}_3$  yield rates are two important descriptors for evaluating the catalytic activity of the NRR process. The  $\text{NH}_3$  yield rate refers to the amount of  $\text{NH}_3$  produced per unit time and unit catalyst mass or area, reflecting the synthesis production rate of  $\text{NH}_3$ . The FE refers to the percentage of charges applied to the NRR process and the total charge flowing, implying the selectivity of  $\text{NH}_3$  synthesis to the competitive HER process.

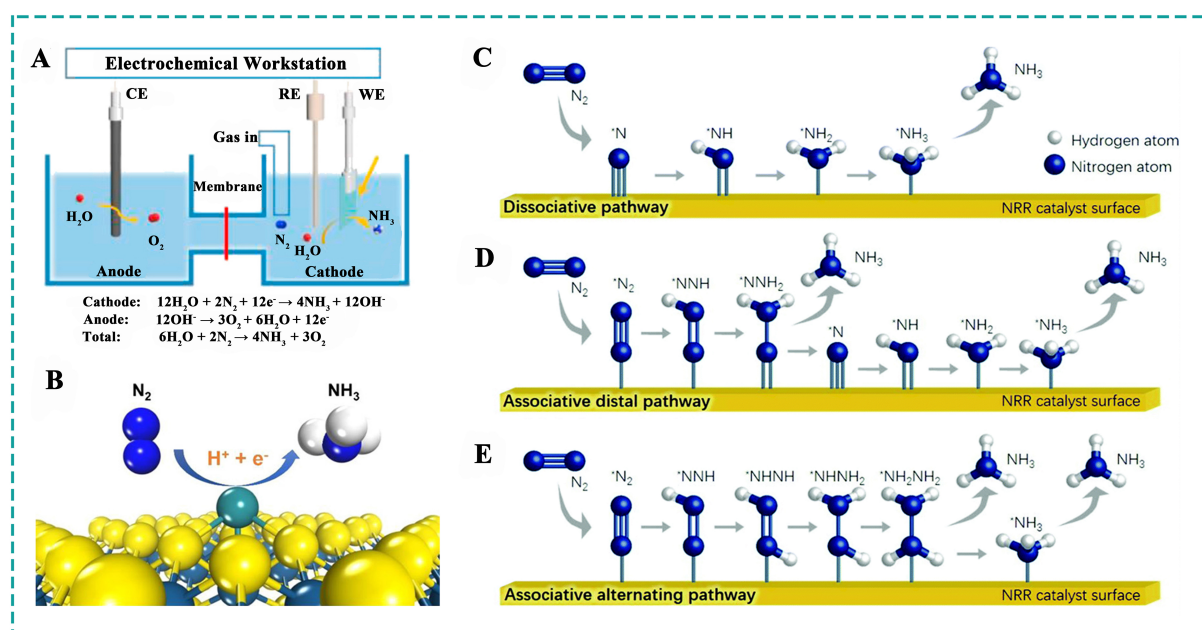


**Figure 2.** (A) The H-type cell of NRR process<sup>[10]</sup>. Copyright 2023, Elsevier; Schematic illustrate of (B) NRR process<sup>[11]</sup>. Copyright 2023, ACS Publications; and (C)–(E) NRR mechanisms, including dissociative pathway, associative distal pathway and associative alternating pathway<sup>[12]</sup>. Copyright 2023, RSC Publishing. NRR: Nitrogen reduction reaction.

The NH<sub>3</sub> yield rate and FE can be calculated by Equations (9) and (10):

$$\text{NH}_3 \text{ yield} = (C_{\text{NH}_3} \times V)/(t \times m) \quad (9)$$

$$FE_{\text{NH}_3} = [3 \times F \times (C_{\text{NH}_3} \times V)]/(17 \times Q) \quad (10)$$

where  $C_{\text{NH}_3}$  is the concentration of NH<sub>3</sub>,  $V$  is the volume of electrolyte,  $t$  is the time of NRR potentiostatic process,  $m$  is the mass of electrocatalyst,  $F$  is Faraday constant ( $96,485 \text{ C}\cdot\text{mol}^{-1}$ ), and  $Q$  is the total charge through the electrodes.

## SYNTHESIS METHODS OF SACS

Selecting appropriate supports to ensure the uniform dispersion of individual metal sites and stabilize them without agglomeration is a prerequisite but a challenge for the preparation of SACs. Developing controllable preparation methods for dispersing atomically active sites on a suitable carrier is crucial to large-scale industrial deployment of SACs. Till now, various approaches have been developed for the fabrication of SACs, such as coordinative pyrolysis, ball milling, chemical/physical deposition, electrochemical deposition, wet-chemistry, defect engineering strategy, and so on.

### High temperature pyrolysis method

High temperature pyrolysis methods are widely applied to synthesize SACs by decomposing the metal precursors at various gas atmospheres (Ar, N<sub>2</sub> or NH<sub>3</sub>)<sup>[16–18]</sup>. Due to their advantages of simple operation and low cost, most carbon-based SACs were prepared using this method from various precursors, such as polymers, metal-organic frameworks (MOFs), metal complexes, and so on. For instance, Wu *et al.* mixed *o*-phenylenediamine and SiO<sub>2</sub> powder with Fe<sup>3+</sup> ions and then pyrolyzed the mixture at 800 °C under Ar temperature to generate the FeN<sub>4</sub> electrocatalysts [Figure 3A and B]<sup>[19]</sup>. K-edge X-ray absorption near edge

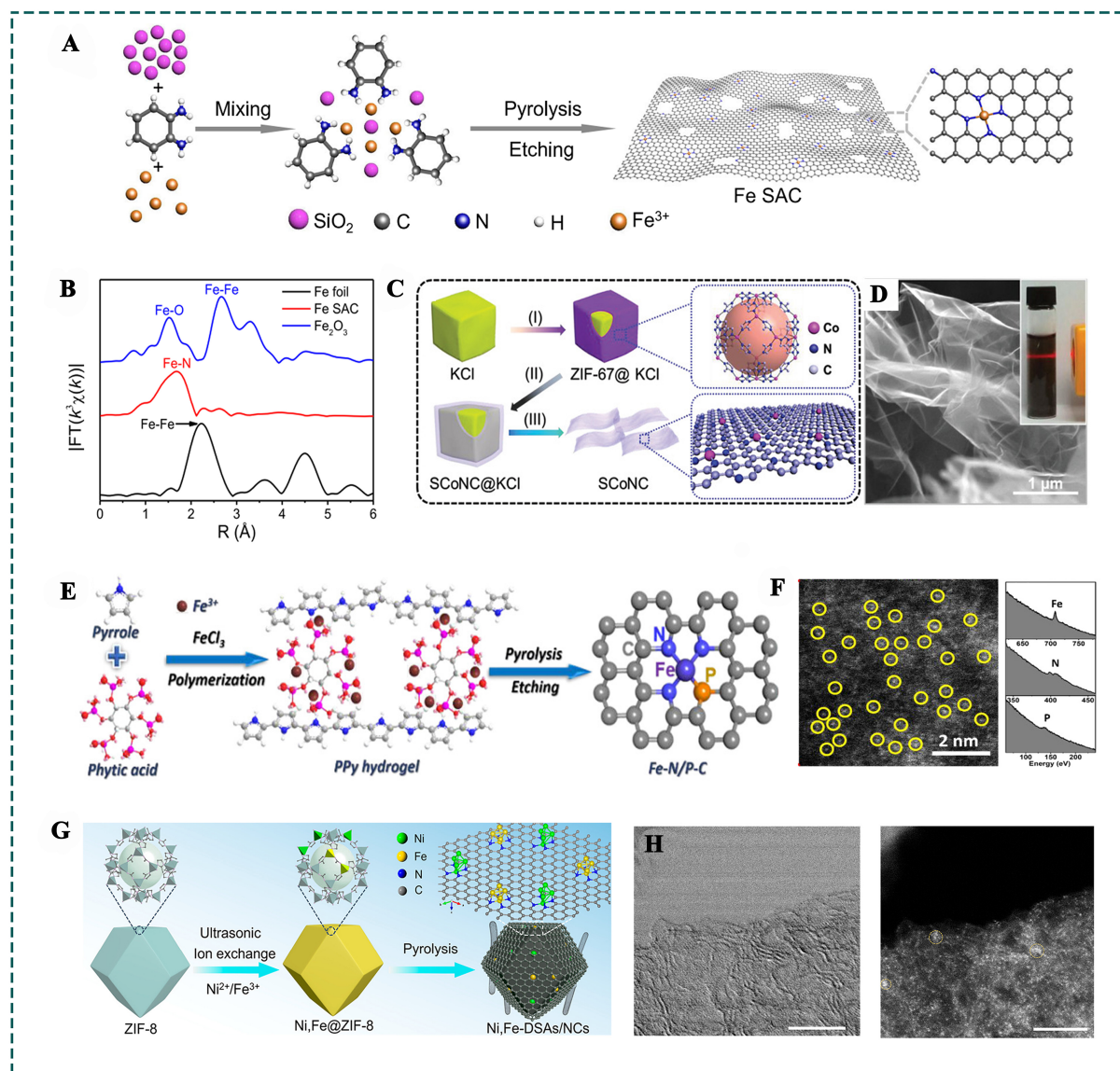


**Figure 3.** (A) Schematic illustration of the synthesis of  $\text{FeN}_4$  SAC; (B) FT  $k^3$ -weighted  $\chi(k)$ -function of the EXAFS spectra at Fe K-edge<sup>[19]</sup>, Copyright 2023, Springer Nature; (C) Schematic illustration of the synthetic procedure of the SCoNC catalysts; and (D) SEM image of the SCoNC catalyst<sup>[20]</sup>. Copyright 2023, Wiley; (E) Schematic of the synthesis process of the Fe-N/P-C catalyst; (F) Enlarged image of Fe-N/P-C, partial single Fe atoms are circled in yellow and EELS atomic spectra of Fe, N, and P elements<sup>[22]</sup>, Copyright 2023, ACS Publications; (G) Synthesis and morphology of Ni,Fe-SAs/NCs; and (H) BF-STEM image and corresponding HAADF-STEM image<sup>[23]</sup>. Copyright 2023, ACS Publications. SAC: Single atom electrocatalyst; EXAFS: extended X-ray absorption fine structure; SEM: scanning electron microscopy; EELS: electron energy loss spectroscopy; NCs: N-doped carbons; BF-STEM: bright field scanning transmission electron microscopy; HAADF-STEM: high-angle annular dark field scanning transmission electron microscopy.

structure (XANES) spectra demonstrated that no Fe–Fe bonds existed in  $\text{FeN}_4$  SACs. Wu *et al.* fabricated a salt-template method by calcinating the mixture of zeolitic imidazolate framework (ZIF)-67 and molten KCl salt at high temperature to prepare the cobalt active sites supported on nitrogen (N)-doped carbon substrate (SCoNC), which achieves a considerably high mass loading of Co atoms ( $\approx 15.3\%$ ) [Figure 3C and D]<sup>[20]</sup>. Rong *et al.* also used the pyrolysis method to prepare Ni- $\text{N}_3\text{O}$  SACs; then, the Ni- $\text{N}_3\text{-V}$  SAC with vacancies could also be obtained by removing the oxygen atoms at 800 °C in view of the weaker Ni–O interaction<sup>[21]</sup>. Yuan *et al.* reported the nitrogen and phosphorous coordinated Fe SAC ( $\text{FeN}_3\text{P}$ ) via calcinating the

polypyrrole (PPy) hydrogel obtained by the polymerization of pyrrole with the assistance of phytic acid and  $\text{FeCl}_3$  [Figure 3E and F]<sup>[22]</sup>. Besides, this method was also extended to design and prepare dual-metal atom catalysts (DACs). Wang *et al.* first synthesized Fe, Ni@ZIF-8 via the ion exchange strategy and then obtained the Ni, Fe-DACs/N-doped carbons (NCs) after calcinating at 920 °C for 3 h [Figure 3G and H]<sup>[23]</sup>. Tamtaji *et al.* reported a series of  $\text{CoN}_4$ ,  $\text{NiN}_4$ ,  $\text{FeN}_4$  SACs, and  $\text{FeNiN}_8$  DACs anchored on graphene oxide (GO) nanosheets<sup>[24]</sup>.

### MOF-derived SACs

MOFs, as porous crystalline materials assembled by metal nodes and organic ligands, have boomed in the last decades due to their large surface area, definite crystalline structure, chemical tunability, and abundant metal sites<sup>[25-28]</sup>. After high temperature pyrolysis using MOFs as precursors, carbon-based SACs can be obtained, and the characteristics of MOFs are also inherited. Especially, the nitrogen elements from the parent MOF enable the formation of strong metal-nitrogen coordination bonds during calcination, thus effectively preventing the aggregation of metal atoms<sup>[29,30]</sup>. Undoubtedly, the MOF-derived nitrogen porous carbon can be applied as an ideal support to stabilize the atomic metal species. Zhao *et al.* prepared the NC supported Ni single atoms (Ni SAs/NC) via the ionic exchange between Zn nodes and the adsorbed Ni ions within the ZIF-8 [Figure 4A]<sup>[31]</sup>. During the carbonization process, the Ni nodes were reduced to Ni SACs, accompanied by the evaporation of low-vaporizing Zn elements. The coordination bonds between NC and metal atoms ensure the tight fixation of metal atoms. Subsequently, using a similar strategy, Fe, Ni single-atom pairs immobilized on NC ( $\text{Fe}_1\text{-Ni}_1\text{-NC}$ ) have been synthesized by Jiao *et al.* [Figure 4B]<sup>[32]</sup>. In the  $\text{Fe}_1\text{-Ni}_1\text{-NC}$  materials, single Fe active sites were activated by the neighboring Ni atoms, thereby alleviating the formation of  $\text{COOH}^\cdot$  intermediate and facilitating the  $\text{CO}_2$  reduction reaction ( $\text{CO}_2\text{RR}$ ).

Apart from ZIF, other MOFs are also employed as expected platforms to stabilize single atoms. Zhao *et al.* designed a two-step strategy to prepare SACs with the single Pd sites anchored on a 3D zirconium oxide nanonet, denoted as  $\text{Pd}_1@ \text{ZrO}_2$ <sup>[33]</sup>. First, the NC supported single Pd sites and  $\text{ZrO}_2$  nanoparticles were obtained by calcination of Zr-based Uio-66- $\text{NH}_2$  under Ar atmosphere. Then, carbonaceous skeletons etched by air and  $\text{ZrO}_2$  were welded into a porous nanonet with rich oxygen defects, which is beneficial for capturing the  $\text{Pd}_1$  species [Figure 4C]. Ma *et al.* reported a microwave method to fabricate Ni SACs with large metal loading (> 4 wt%) and tunable coordination environment, which were also expanded to Co and Cu SACs, respectively<sup>[34]</sup>. With the help of uncoordinated  $-\text{NH}_2$ , the Ni atoms were stably immobilized on the Uio-66- $\text{NH}_2$ . By varying the treatment procedures, the coordination environments of SACs are well optimized to obtain the  $\text{Ni}_1\text{-X/Uio-66-NH}_2$  (X means S, O, or  $\text{S}_{\text{ox}}$ ) [Figure 4D]. Among those, the sulfur-coordinated Ni centers exhibit the best photocatalytic activity due to their reductive oxidation state. The Pt active sites were also successfully stabilized in Al-TCPP via the tight bonding between the pyrrolic N of Al-TCPP and Pt atoms [Figure 4E]. The obtained Pt SACs give rise to a  $\text{H}_2$  turnover frequency (TOF) of  $35 \text{ h}^{-1}$ , which is 30 times that of Pt nanoparticles stabilized by the same Al-TCPP. The confinement of Pt atoms into MOFs, which offers convenient electron transfer pathways and enhanced hydrogen binding energy, can account for the outstanding photocatalytic performance<sup>[35]</sup>. MOF-based SACs combined the advantages of MOF and SACs, exhibiting outstanding performance in various catalytic reactions. Nevertheless, developing a facile and economic synthesis procedure for MOF-based SACs and further increasing the mass loading of SACs remains challenging.

### Impregnation and coprecipitation strategy

The impregnation and coprecipitation strategy have been the widespread method for synthesizing SACs due to its simpleness, high repetition, and no requirement on special equipment. The typical coprecipitation method generally includes the following steps: (i) mixing anions and cations in the solution; (ii) nucleation and growth; (iii) aggregation and coprecipitation. The obvious advantage of this method is that two or more

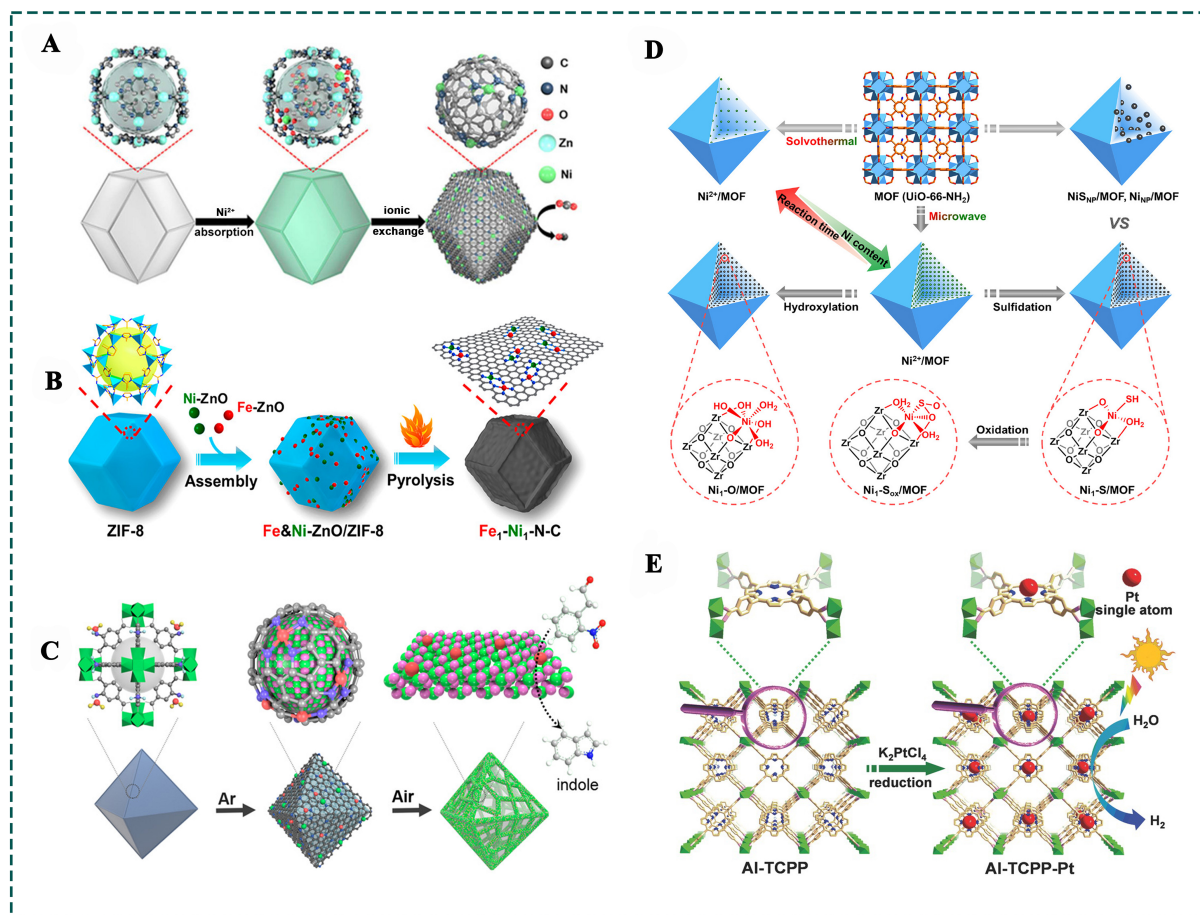


**Figure 4.** (A) Scheme of the formation of Ni SAs/N-C<sup>[31]</sup>. Copyright 2023, ACS Publications; (B) Schematic Illustration for Construction of Fe<sub>x</sub>Ni<sub>y</sub>N-C with Neighboring Fe and Ni Single-Atoms Based on ZIF-8<sup>[32]</sup>. Copyright 2023, ACS Publications; (C) Schematic illustration of synthetic route of Pd<sub>x</sub>@ZrO<sub>2</sub><sup>[33]</sup>. Copyright 2023, ACS Publications; (D) Schematic illustration showing Ni<sup>2+</sup> decoration in UiO-66-NH<sub>2</sub> via an efficient microwave-assisted method and the subsequent coordination environment modulation of single Ni Atoms to afford Ni<sub>i</sub>-X/MOF<sup>[34]</sup>. Copyright 2023, ACS Publications; (E) Schematic illustration showing the synthesis of Al-TCPP-Pt for photocatalytic hydrogen production<sup>[35]</sup>. Copyright 2023, Wiley. SAs: Single atoms; ZIF: zeolitic imidazolate framework; MOF: metal-organic framework.

cations can be simultaneously precipitated during the chemical reactions, and one or more metal atoms can be uniformly distributed in the catalysts. Nevertheless, during the precipitation process, the aggregation of metal atoms usually occurs, which is influenced by preparation conditions, including pH, temperature and cation concentration<sup>[36,37]</sup>. Therefore, ensuring the metal atomic dispersion remains a challenge. Yang *et al.* prepared the atomically dispersed Ru decorated on two-dimensional NiFe LDH nanosheets (<sup>SA</sup>Ru/NiFe LDH) through wet impregnation<sup>[38]</sup>. In the process, the RuCl<sub>3</sub> as a metal precursor and NaBH<sub>4</sub> as a reduction agent were mixed with the NiFe LDH. It is confirmed that Ru single active sites were stabilized on NiFe LDH through the Ru-O coordinated bond. Using this strategy, the Au/Ce<sub>0.5</sub>Zr<sub>0.5</sub>O<sub>2</sub> catalysts were also prepared. In a typical process, Ce<sub>0.5</sub>Zr<sub>0.5</sub>O<sub>2</sub> support was impregnated in the HAuCl<sub>4</sub> solution with adjusting the pH to 7 by the Na<sub>2</sub>CO<sub>3</sub>, and HAuCl<sub>4</sub> was precipitated and loaded onto the Ce<sub>0.5</sub>Zr<sub>0.5</sub>O<sub>2</sub> support<sup>[39]</sup>.

### Single atom alloys

Single atom alloys (SAAs), with the individual metal sites anchored on another metal host, have emerged as a new hotspot because they simultaneously have the merits of SACs and metal alloys<sup>[40,41]</sup>. Besides that, the alloying effect of SAAs results in strong metal-support interaction, enabling the regulation of the *d*-band

structure of active centers and the balancing of the dissociation and adsorption of intermediates, leading to expected catalytic activity and high selectivity<sup>[6,42]</sup>. More importantly, the tenacious alloy bonding between isolated metal atoms and the metal host would effectively inhibit the agglomeration of metal atoms during the catalysis process and allow for powerful control over the individually atomic dispersion.

Using this strategy, a series of SAAs catalysts applied in various electrocatalytic reactions have been fabricated in recent years<sup>[43-46]</sup>. Wang *et al.* prepared bimetallic Pd@Au electrocatalysts by decorating Au nanoparticles with controlled Pd atoms via the reduction of PdCl<sub>2</sub> with 5% H<sub>2</sub>/N<sub>2</sub> at room temperature [Figure 5A]<sup>[46]</sup>. The morphology of Pd@Au alloys can be tuned from Pd single atomic dispersion to core-shell when the contents of Pd elements range from 2% to 20%. Chen *et al.* reported the RuAu SAAs using a laser ablation strategy by immersing Ru target in HCl and HAuCl<sub>4</sub> solution<sup>[47]</sup>. Profiting from the strong quenching effect, metastable RuAu nanostructures with novel properties are obtained and the Au atom content can be reached as high as 36.53 at%. Jiao *et al.* introduced Pd and Cu elements onto Te nanowires through a galvanic replacement technique [Figure 5B and C]<sup>[48]</sup>. Derived from the unique structure of the substrate, the Cu<sub>1</sub><sup>0</sup>-Cu<sub>1</sub><sup>x+</sup> pairs with different charges were successfully immobilized in Pd<sub>10</sub>Te<sub>3</sub> alloy nanowires after an alkaline and acid washing process. In addition, the SSAs have also been applied in the NRR field. Muravev *et al.* employed CeO<sub>2</sub> nanorod as metal platforms to immobilize the Pd single atoms via a frame spray pyrolysis strategy [Figure 5D]<sup>[49]</sup>. The surface Pd single atoms displayed a high resistance against sintering. In addition, density functional theory (DFT) and extended X-ray absorption fine structure (EXAFS) revealed that the isolated Pd ions activates the lattice oxygen of the CeO<sub>2</sub> support and facilitates an oxygen spillover at the Pd-O-Ce interface.

### Electrochemical deposition

Electrochemical deposition strategy has been widely employed to fabricate SACs on support materials due to its simple and clean characteristics. Zhang *et al.* proposed a universal electrochemical deposition strategy to synthesize SACs on different matrices, including metal, metal hydroxide, or metal sulfide. Through controlling the deposition times and cycles, the concentration of metals can be varied<sup>[50]</sup>. Zhang *et al.* prepared NiFe LDH on the surface of Ti foil first, which was subsequently employed as the working electrode in the HAuCl<sub>4</sub> solution. After stepping the potential to -0.6 V for 5 s and to -0.2 V for 5 s repeated for five cycles, isolated Au atoms were anchored on NiFe LDH<sup>[51]</sup>. Xu *et al.* reported the Cu single atoms immobilized on sulfur sites of graphite foam via an underpotential deposition strategy [Figure 6A]. By varying the electrodeposition potentials and the sulfur contents of graphite foam, the loading amount of Cu SAs can be regulated from 0.043% to 0.3% [Figure 6B]<sup>[52]</sup>. In addition, the counter electrode containing the target metals can also directly act as the counter electrode for the deposition. For example, Mo<sub>2</sub>TiC<sub>2</sub>T<sub>x</sub> MXene was employed as the platform to deposition Pt with the Pt foil as the counter electrode. During the process, MXene is originally exfoliated to nanosheets with the Mo atoms leaving the MXene, and the Pt atoms that detached from the Pt foil simultaneously moved to the working electrode and filled into the Mo vacancies [Figure 6C and D]<sup>[53]</sup>. Using the same method, Jiang *et al.* successfully removed the Co atoms from the np-Co<sub>0.85</sub>Se to form Co vacancies with Pt foil as the counter electrode in 0.5 M H<sub>2</sub>SO<sub>4</sub> solution which act as a trapper for embedding the Pt atoms<sup>[54]</sup>.

### Atomic layer deposition

Atomic layer deposition (ALD) is a recently emerging method to prepare SACs, which needs the target metal precursors in the gas state and to be carried in the substrate in the reaction chamber. The size and thickness of deposition layers could be well tuned by regulating the deposition times and cycles<sup>[55-57]</sup>. Song *et al.* prepared individually Ir modified Pt nanoparticles supported on the NC nanotube (Ir<sub>SA</sub>-Pt/NCNT) via an ALD approach. The Ir<sub>SA</sub>-Pt catalyst, with the combination of SA and nanoparticle (NP) cooperation structure, shows promoted catalytic activity and stability toward both oxygen evolution reaction (OER) and

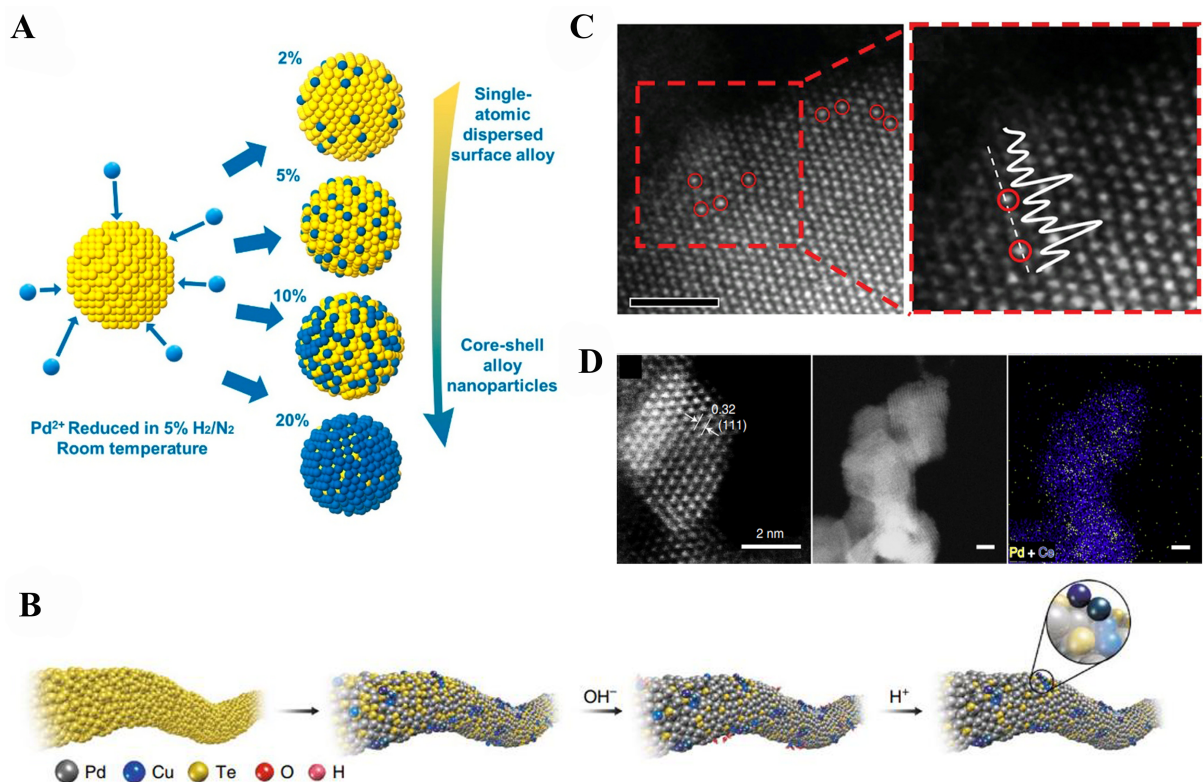


**Figure 5.** (A) Illustration of the synthetic scheme for the Pd@Au nanoparticles with control over the dose of Pd<sup>[46]</sup>. Copyright 2023, ACS Publications; (B) Schematic illustration of the fabrication procedures of atom-pair structured Cu anchored on Pd<sub>10</sub>Te<sub>3</sub> nanowires<sup>[48]</sup>. Copyright 2023, Springer Nature; (C) Atomic-resolution HAADF-STEM image. Au atoms are uniformly distributed throughout the particle. Scale bar: 1 nm<sup>[47]</sup>. Copyright 2023, Wiley; (D) HAADF-STEM and EDX-mapping images of Pd-CeO<sub>2</sub> nanorod<sup>[49]</sup>. Copyright 2021, Springer Nature. HAADF-STEM: High-angle annular dark field scanning transmission electron microscopy.

oxygen reduction reaction (ORR)<sup>[58]</sup>. Using this strategy, atomically dispersed Co on Pt catalysts were also prepared by Zhang *et al.*<sup>[59]</sup>. Li *et al.* anchored atomically dispersed Pt on C<sub>3</sub>N<sub>4</sub> nanosheets with ALD strategy. By adjusting the deposition cycles, they controlled the size of Pt to obtain Pt SAs, Pt clusters and Pt nanoparticles, respectively<sup>[57]</sup>. Besides that, the ALD strategy can also be used to synthesize the 2D materials<sup>[60,61]</sup>. Yan *et al.* fabricated two atomic layer thickness of Pt layers onto the graphene by depositing the second atomic layer on the former first atomic layer<sup>[61]</sup>.

## HOW TO REGULATE THE CATALYTIC PERFORMANCE OF SACS

The microenvironments of SACS, such as coordination environment, band structure, and geometric construction, are decisive on regulating chemical properties and optimizing catalytic performance of SACS. Therefore, constructing SAC catalysts with well-controlled configuration and homogeneous dispersion is essential to exploring the relationship between the intrinsic activity of the catalysts and the structure characterization.

### Coordination components

It is well known that the catalytic activity of catalysts is largely decided by the local metal coordination environment<sup>[62-64]</sup>. Clarifying the structure-function relationship between the coordination environment of active metal sites and the catalytic activity is crucial to achieving high performance SAC catalysts and demonstrating the reaction mechanism. The active metal sites were generally coordinated by nonmetal

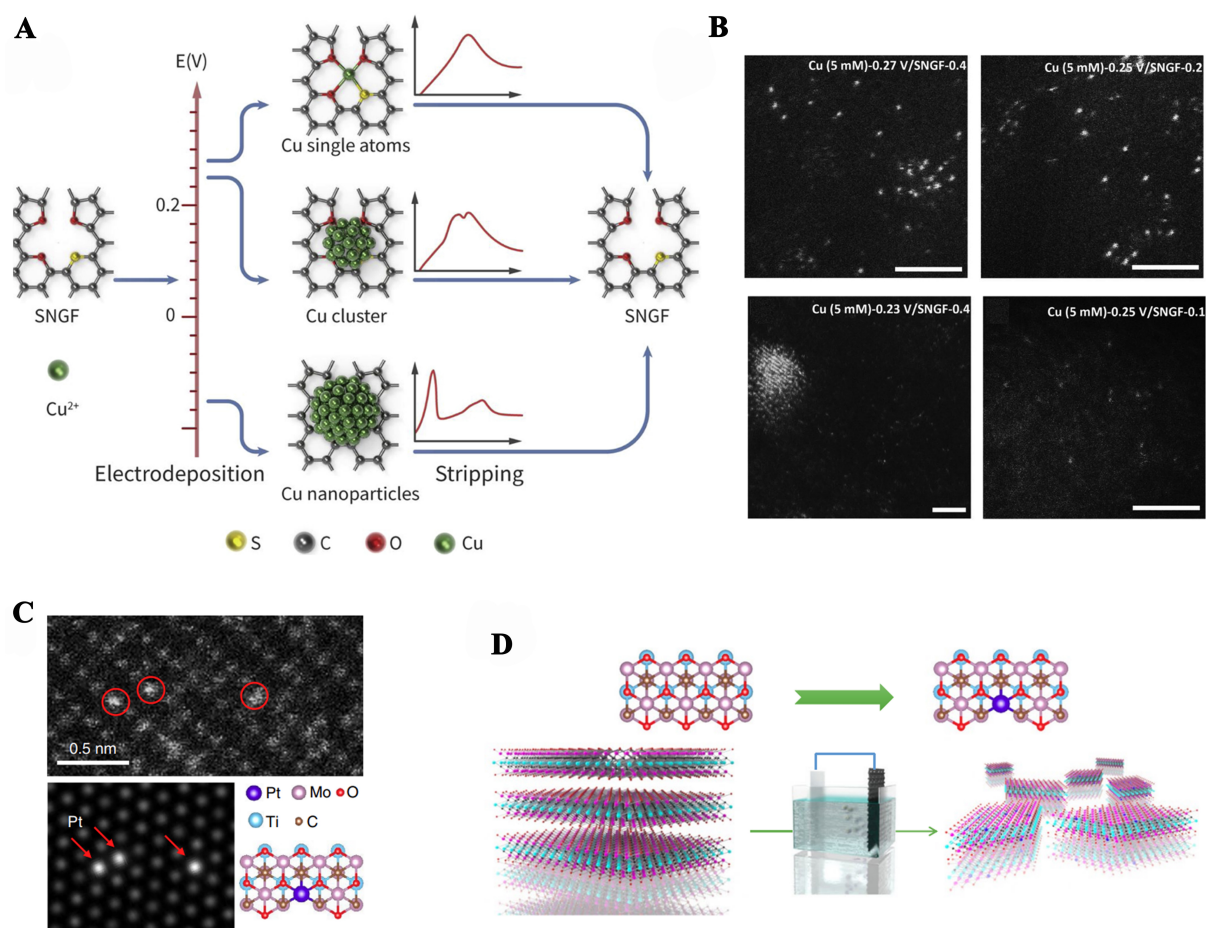


**Figure 6.** (A) Schematic illustration of electrochemical synthesis/analysis of Cu SACs; (B) HAADF-STEM images of Cu SAs and Cu nanoparticles by adjusting the deposition potential and concentration of Cu precursors<sup>[52]</sup>. Copyright 2023, Elsevier; (C) HAADF-STEM images of  $\text{Mo}_2\text{TiC}_2\text{T}_x\text{-Pt}_{\text{SA}}$  and corresponding simulated image; (D) Schematic of the electrochemical exfoliation process of MXene with immobilized single Pt atoms<sup>[53]</sup>. Copyright 2023, Springer Nature. SACs: Single atom electrocatalysts; HAADF-STEM: high-angle annular dark field scanning transmission electron microscopy; SAs: single atoms.

atoms, such as N, O, S, P, *etc.*<sup>[22,65-67]</sup>. Therefore, regulating and optimizing the coordination nonmetal atoms and coordination number will reconstruct the coordination environment and thus adjust the electronic and band structure of metal sites. As a result, the catalytic activity would be effectively improved by precisely designing the environment atoms of SACs.

Based on above theoretical guidance, researchers have denoted enormous efforts in verifying the role of micro coordination environment in the electrochemical performance from the experiment point<sup>[68]</sup>. Zhang *et al.* have introduced N species into the isolated Ni atoms<sup>[69]</sup> [Figure 7A and B]. They reported that the Ni-N coordination has lower Fermi level and stronger adsorption of intermediates compared with Ni-C coordination [Figure 7C]. Jiang *et al.* also reported a similar phenomenon in the  $\text{FeN}_4$  SACs, in which the N-C bond of the Fe-N<sub>4</sub>-C active sites can be selectively broken and the remaining Fe-N<sub>4</sub> sites exhibit an excellent catalytic activity<sup>[70]</sup>. Furthermore, Cai *et al.* fabricated  $\text{CuN}_2\text{O}_2$  SACs to optimize the electronic structure of copper active sites via a partial-carbonization strategy for the first time [Figure 7D]<sup>[71]</sup>. They reported that the Cu atoms of  $\text{CuN}_2\text{O}_2$  possess a low-valent oxidation state compared to  $\text{CuN}_x$ , which is beneficial for lowering adsorption energy of  $^*\text{COOH}$  intermediate and inhibiting the  $^*\text{H}$  adsorption, thus

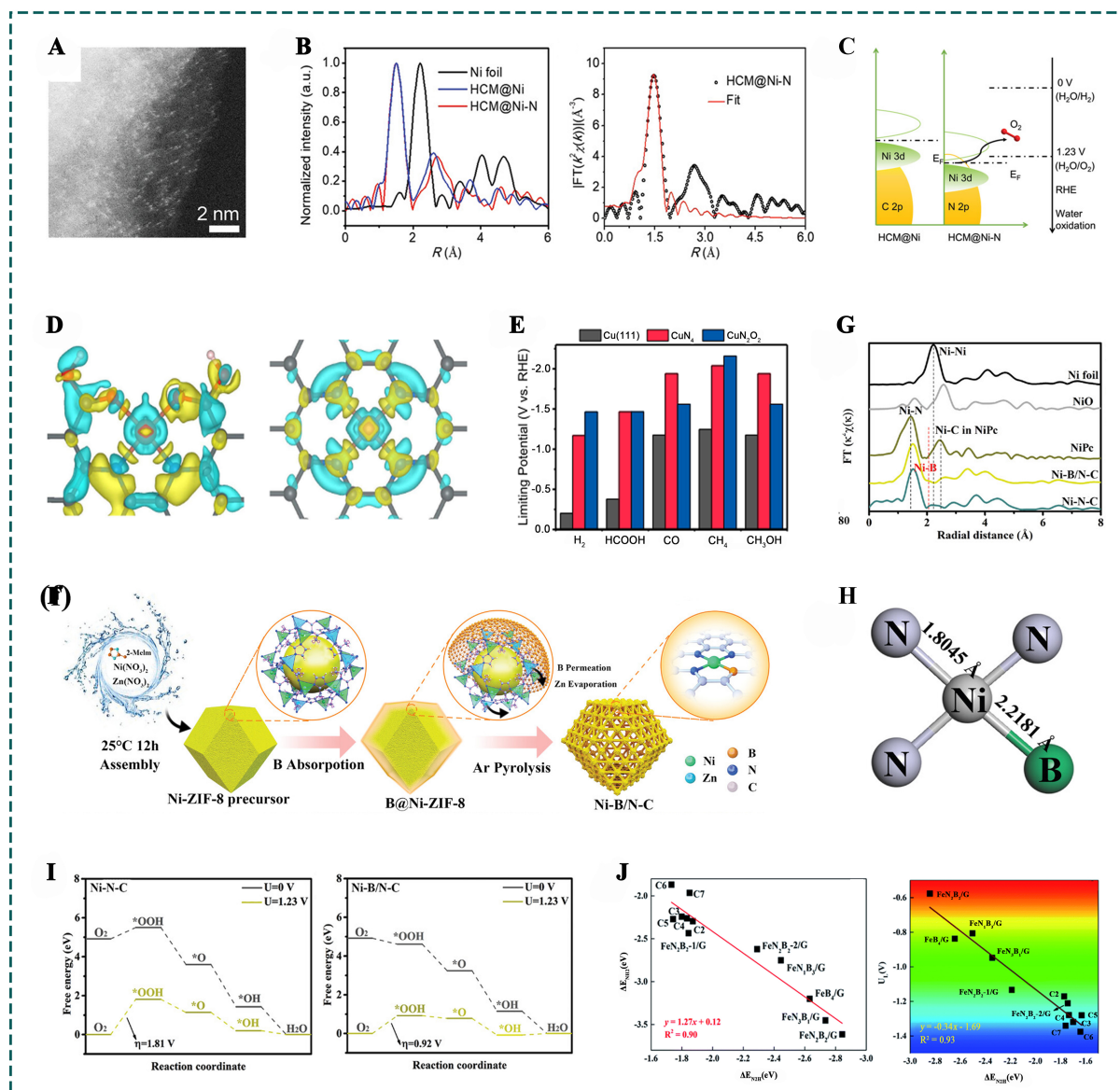


**Figure 7.** (A) The atomic resolution HAADF-STEM image of HCM@Ni-N; (B) Ni K-edge EXAFS spectra and Fourier transform of the experimental EXAFS spectrum in K space of HCM@Ni-N; (C) Schematic band diagrams of HCM@Ni and HCM@Ni-N<sup>[69]</sup>. Copyright 2023, Wiley; (D) Differential charge densities of Cu<sub>2</sub>O<sub>2</sub> and CuN<sub>4</sub>; (E) The limiting potentials of the products of ECR and HER on the CuN<sub>2</sub>O<sub>2</sub>, CuN<sub>4</sub>, and Cu(111)<sup>[71]</sup>. Copyright 2023, Springer Nature; (F) Schematic diagram of the preparation process of Ni-B/N-C; (G) The FT EXAFS spectra of Ni foil, NiO, NiPc, Ni-B/N-C, and Ni-N-C; (H) Coordination environment of Ni-B<sub>3</sub>N<sub>3</sub> moiety; (I) Gibbs free energy diagram for ORR process of the Ni-N<sub>4</sub> and Ni-B<sub>1</sub>N<sub>3</sub> moiety<sup>[72]</sup>. Copyright 2023, Wiley; (J) The scaling relationships for the adsorption energy of NH<sup>-</sup>-N<sub>2</sub>H<sup>+</sup> and Linear correlations between the adsorption energy of N<sub>2</sub>H<sup>+</sup> (E<sub>N<sub>2</sub>H<sup>+</sup></sub>) and limiting potential of the NRR<sup>[73]</sup>. Copyright 2023, RSC Publishing. HAADF-STEM: High-angle annular dark field scanning transmission electron microscopy; EXAFS: extended X-ray absorption fine structure; ECR: CO<sub>2</sub> reduction reaction; HER: hydrogen evolution reaction; ORR: oxygen reduction reaction; NRR: nitrogen reduction reaction.

improving the catalytic activity and selectivity [Figure 7E and F]. Wang *et al.* fabricated boron and nitrogen dual-coordinated SACs by calcinating the Ni-ZIF-8 with the presence of B sources [Figure 7G]<sup>[72]</sup>. The local atomic coordination structure of the Ni-B/N-C catalyst was characterized by X-ray absorption fine structure (XAFS). From Figure 7H, it can be revealed that the central Ni atom was coordinated with three N atoms and one B atom with the bond lengths of 1.80 and 2.21 Å, respectively [Figure 7I]. This unique coordination

structure ensures the stronger coupling between the central Ni site and the adsorbed O species in comparison with NiN<sub>4</sub> active centers, thus endowing them with enhanced ORR activity [Figure 7]. Jiao *et al.* have also demonstrated the effects of coordination environment of Fe-N-C on NRR activity via DFT computations. They constructed the FeB<sub>1</sub>N<sub>3</sub>/G, FeB<sub>2</sub>N<sub>2</sub>/G, FeB<sub>3</sub>N<sub>1</sub>/G, and FeB<sub>4</sub>/G, respectively, by replacing the coordinated N atoms with B atoms. The FeB<sub>2</sub>N<sub>2</sub>/G displays the highest NRR activity; this is mainly due to the fact that the introduction of B can effectively modulate the interaction of the single Fe atom with the N<sub>2</sub>H<sup>+</sup> species<sup>[73]</sup>.

### Coordination number of active sites

Besides, regulating the coordination number of isolated active centers has also been a feasible means of modulating the intrinsic activity of SACs<sup>[21,74-76]</sup>. Liu *et al.* have synthesized dispersed Fe active sites with different coordination numbers (FeN<sub>x</sub>, x = 4-6) by controlling the treatment temperature [Figure 8A-C]<sup>[74]</sup>. It is demonstrated that the medium-spin Fe<sup>III</sup>N<sub>5</sub> affords the highest TOF for oxidation of C-H, which is one order of magnitude of the Fe<sup>III</sup>N<sub>6</sub> structures and three times more active than the Fe<sup>II</sup>N<sub>4</sub> structure, respectively. Rong *et al.* also fabricated vacancy-defect Ni-N<sub>3</sub>-V sites anchored on the GO nanosheets [Figure 8D and E]<sup>[21]</sup>. Experiment results and DFT calculations clarified that Ni-N<sub>3</sub> site has played a vital role in boosting CO<sub>2</sub>RR activity by lowering the energy barrier to form COOH<sup>+</sup> intermediate. The TOF value of CO<sub>2</sub> reduction for Ni-N<sub>3</sub>-V is 1.35 × 10<sup>5</sup> h<sup>-1</sup>, which is four times that of Ni-N<sub>4</sub> (3.46 × 10<sup>4</sup> h<sup>-1</sup>). Zhang *et al.* have also investigated the effect of coordination number for active centers in lithium-sulfur (Li-S) batteries to address the issues of shuttle effect and sluggish electrochemical kinetics of lithium polysulfides (LiPSs) [Figure 8F and G]<sup>[77]</sup>. They prepared Ni-N<sub>3</sub>, Ni-N<sub>4</sub>, and Ni-N<sub>5</sub> catalysts with different coordination numbers and proved that the Ni-N<sub>5</sub> exhibits faster LiPSs conversion kinetics and stronger chemical bonding between Ni sites and the sulfur elements in the L<sub>2</sub>S<sub>6</sub>.

### Metal-support interaction

Electronic metal-support interaction is a promising approach to regulate the electronic structure of metal active sites via the covalent bond effect with the supports<sup>[78,79]</sup>. In these materials, orbital hybridization and electron transfer occur on the metal-support interfaces, which can form new bonds and effectively modulate the *d*-electron status of metal active sites<sup>[80-82]</sup>. The related electron configuration will enhance the chemisorption and activation of reaction species and hence lower the energy barrier in the overall reaction process, thus facilitating the catalytic performance. For instance, Hu *et al.* realized the stabilization of isolated Pd species on different crystals of CeO<sub>2</sub> [Figure 9A]<sup>[83]</sup>. X-ray absorption spectroscopy (XAS) results demonstrate that Pd species are well trapped by the oxygen vacancy of the (100) facet for CeO<sub>2</sub>, whereas Pd atoms would aggregate into clusters on the (111) facet [Figure 9B]. Shi *et al.* have immobilized Pt single atoms on various transition metal sulfides (TMDs) supports (TMDs: MoS<sub>2</sub>, WS<sub>2</sub>, MoSe<sub>2</sub>, and WSe<sub>2</sub>) to reveal the structure-activity relationship of SACs. They found that the oxidation state of Pt sites could be well controlled through the electronic metal-support interaction, delivering positive relationship with the Pt-OH interaction. Meanwhile, the alkaline HER activity showed a volcano-type relationship [Figure 9C-F]<sup>[84]</sup>. Recently, Qu *et al.* have proposed a facile strategy to contrast SACs by trapping transition metal atoms (Fe, Co, Ni and Cu) with the dangling bonds on GO. The electron transfer between M<sup>0</sup> and the oxygen-containing functional groups gives rise to the isolated M<sup>δ+</sup> (0 < δ < 3) species by forming M-O bands [Figure 9G-J]<sup>[85]</sup>.

### Spatial microenvironment regulation

Spatial microenvironment has been considered as an effective strategy to synthesize SACs with regulated catalytic activity and selectivity. Hu *et al.* developed a MOF-assisted spatial confinement strategy for confining Ru atoms into the N-doped porous carbon, having an important effect on the internal affinity of Li<sub>2</sub>O<sub>2</sub> [Figure 10A]<sup>[86]</sup>. Liu *et al.* have stabilized individually dispersed Mo into the pores of the molecular

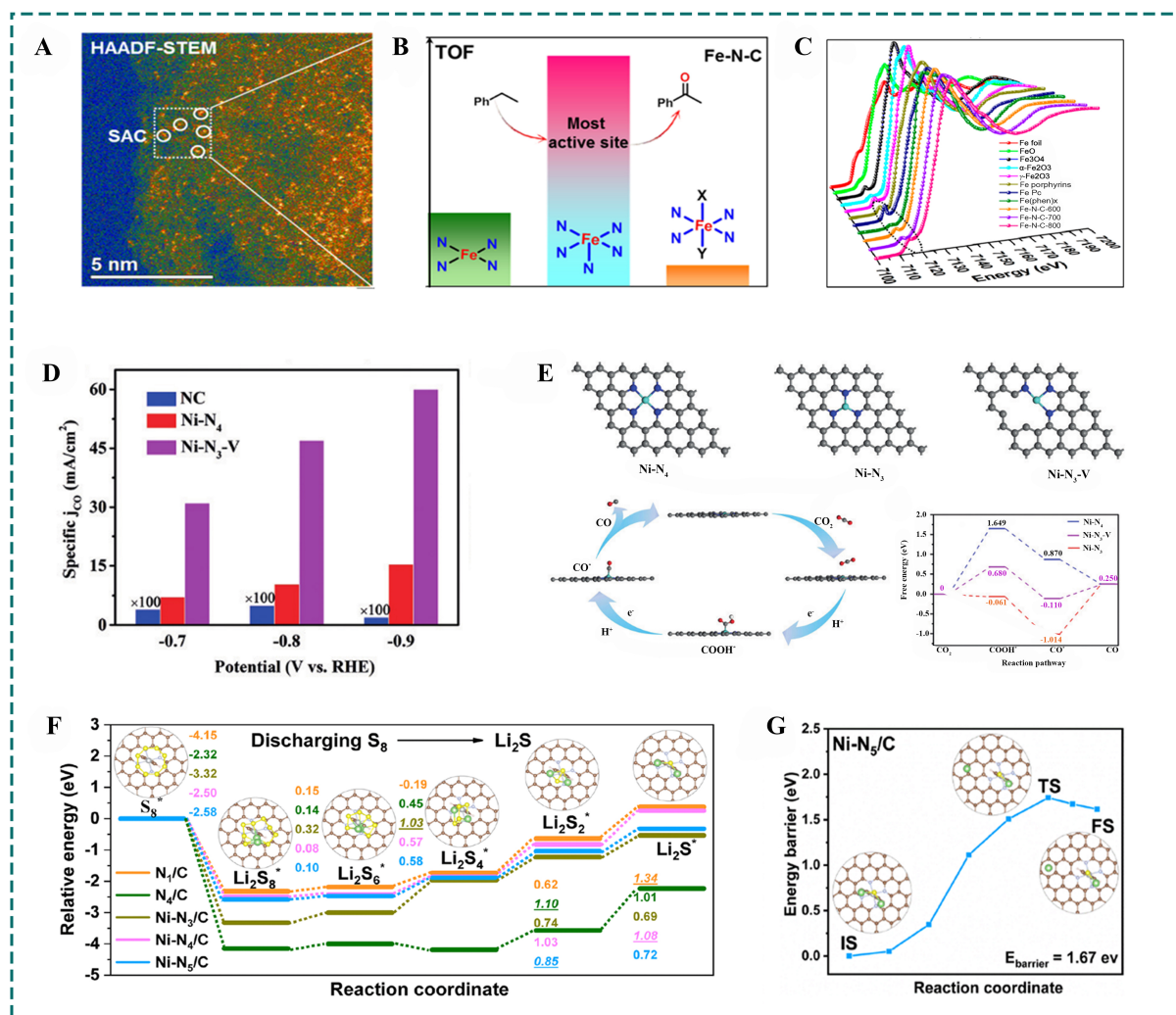


**Figure 8.** (A) HAADF-STEM images of Fe-N-C; (B) The TOF of different sites; (C) The normalized XANES spectra at the Fe K-edge of different samples<sup>[74]</sup>. Copyright 2023, ACS Publications; (D) Specific current density of CO for Ni-N<sub>3</sub>-V, Ni-N<sub>4</sub> and NC; (E) The optimized structures of Ni SACs and the proposed reaction pathways of Ni-N<sub>3</sub>-V for CO<sub>2</sub> electroreduction to CO<sup>[21]</sup>. Copyright 2023, Wiley; (F) Energy profiles for the discharging process from S<sub>8</sub> to Li<sub>2</sub>S on the five catalyst models; (G) Energy profiles for the reduction of Li<sub>2</sub>S on Ni-N<sub>5</sub>/C<sup>[77]</sup>. Copyright 2023, ACS Publications. HAADF-STEM: High-angle annular dark field scanning transmission electron microscopy; TOF: turnover frequency; XANES: X-ray absorption near edge structure; SACs: single atom electrocatalysts.

sieve ZSM-5 matrix<sup>[87]</sup>. The integrated differential phase-contrast scanning transmission electron microscopy (iDPC-STEM) image verifies the dispersion of Mo single species [Figure 10B and C]. The Pt atoms were also successfully anchored in Al-TCPP via the tight bonding between the pyrrolic N of Al-TCPP and Pt atoms<sup>[35]</sup>. Chen *et al.* have embedded the N-heterocyclic carbene (NHC)-ligated Cu SAs into UiO-67. The  $\sigma$  donation of NHC enriches the electron density of SAs and promotes the adsorption of carbon containing intermediates during the CO<sub>2</sub>RR process [Figure 10D and E]<sup>[88]</sup>.

Defects or vacancies are also usually applied to stabilize the single atoms, which play a positive effect in optimizing the electrochemical performance of SACs. Controlled design of defects or vacancies on support is considered as an effective way to prepare SACs with regulated microenvironment. Zhang *et al.* have implanted atomic PtCo on the defect C/N graphene surface to generate Co-Pt-N-C coordination structure as active centers for ORR [Figure 10F]<sup>[27]</sup>. Liu *et al.* have confined isolated Pd species on C<sub>3</sub>N<sub>4</sub> by the

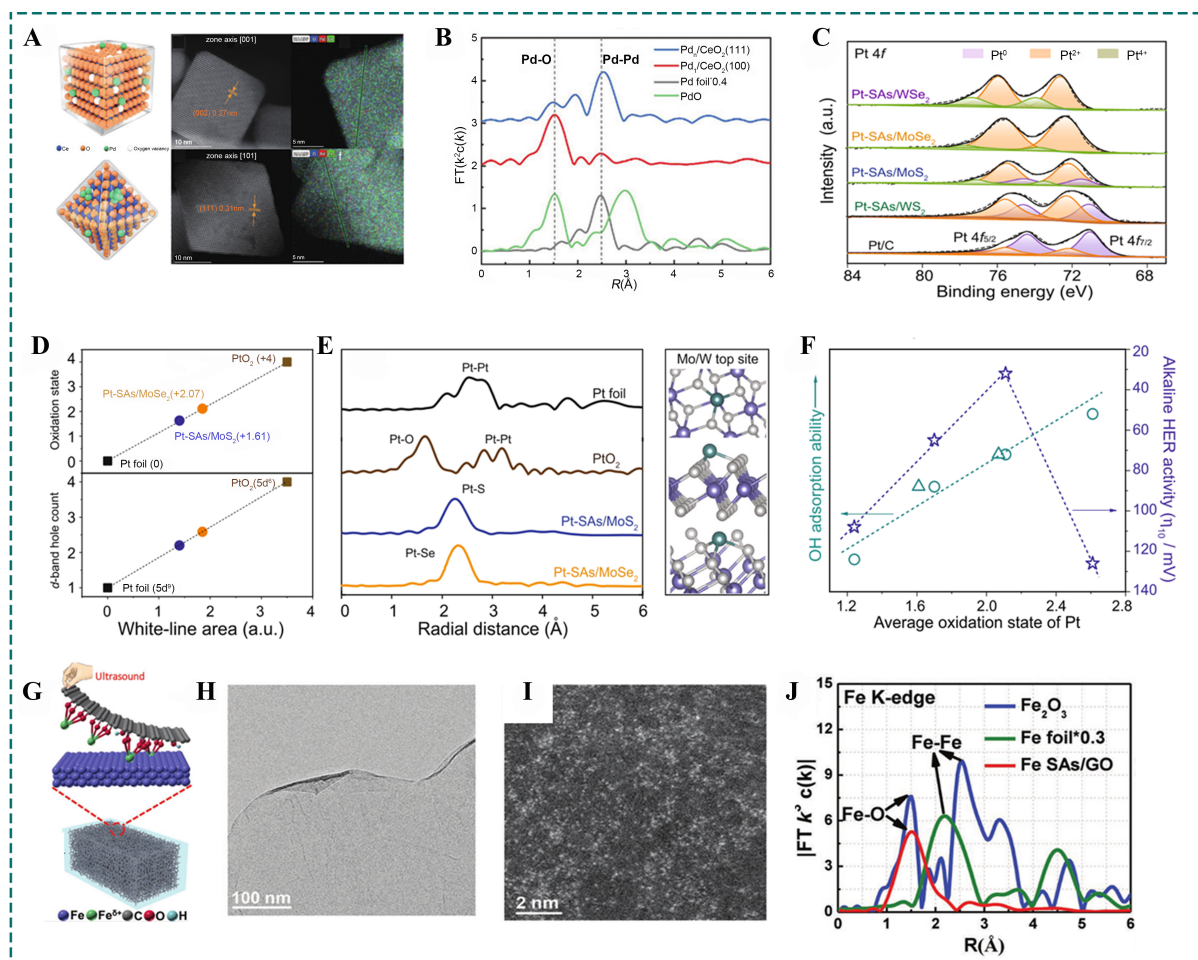


**Figure 9.** (A) Structural models and HAADF-STEM images of Pd<sub>v</sub>/CeO<sub>2</sub>(100) and Pd<sub>n</sub>/CeO<sub>2</sub>(111); (B) Fourier transforms of k<sub>3</sub>-weighted Pd K-edge EXAFS spectra<sup>[83]</sup>. Copyright 2023, Wiley; (C) Pt 4f XPS spectra of the Pt-SAs/TMDs samples and commercial Pt/C; (D) The fitted average oxidation states and *d*-band hole counts of Pt from XANES spectra; (E) First-shell fitting of EXAFS spectra of Pt foil, PtO<sub>2</sub>, Pt-SAs/MoS<sub>2</sub>, and Pt-SAs/MoSe<sub>2</sub>; (F) Relationship of average oxidation state, Pt-OH interaction and alkaline HER activity of PtSAs/TMDs<sup>[84]</sup>. Copyright 2023, Springer Nature; (G) Schematic illustration for the preparation of Fe SAs/GO; (H) TEM and (I) HAADF-STEM images of Fe SAs/GO; (J) EXAFS spectra of Fe SAs/GO<sup>[85]</sup>. Copyright 2023, Wiley. HAADF-STEM: High-angle annular dark field scanning transmission electron microscopy; EXAFS: extended X-ray absorption fine structure; TMDs: transition metal sulfides; XANES: X-ray absorption near edge structure; SAs: single atoms; HER: hydrogen evolution reaction; GO: graphene oxide; TEM: transmission electron microscopy.

abundant carbon vacancies for photocatalytic NO conversion. High-angle annular dark field scanning transmission electron microscopy (HAADF-STEM) and XAFS analyses confirm that the Pd atoms prefer to be trapped on carbon vacancy sites. The activity of Pd-Cv-CN is approximately 4.4 times of Pd loaded on pristine g-C<sub>3</sub>N<sub>4</sub> [Figure 10G]<sup>[89]</sup>. Su *et al.* also confined isolated Fe sites with N vacancies and proved that the N vacancies act as electron trap sites to form highly concentrated electron density around Fe sites for improving the H<sub>2</sub>O<sub>2</sub> conversion efficiency [Figure 10H]<sup>[90]</sup>. Kumar *et al.* have realized the ultrahigh loading of Rh atoms (6.6 wt%) on Co<sub>3</sub>O<sub>4</sub> nanolayers with tensile strain (S-Co<sub>3</sub>O<sub>4</sub>) obtained through liquid N<sub>2</sub>-quenching. A significantly increased migration energy barrier of Rh<sub>SA</sub> on the S-Co<sub>3</sub>O<sub>4</sub> is revealed than on pristine Co<sub>3</sub>O<sub>4</sub>, which inhibits the migration and aggregation of Rh atoms<sup>[91]</sup>.

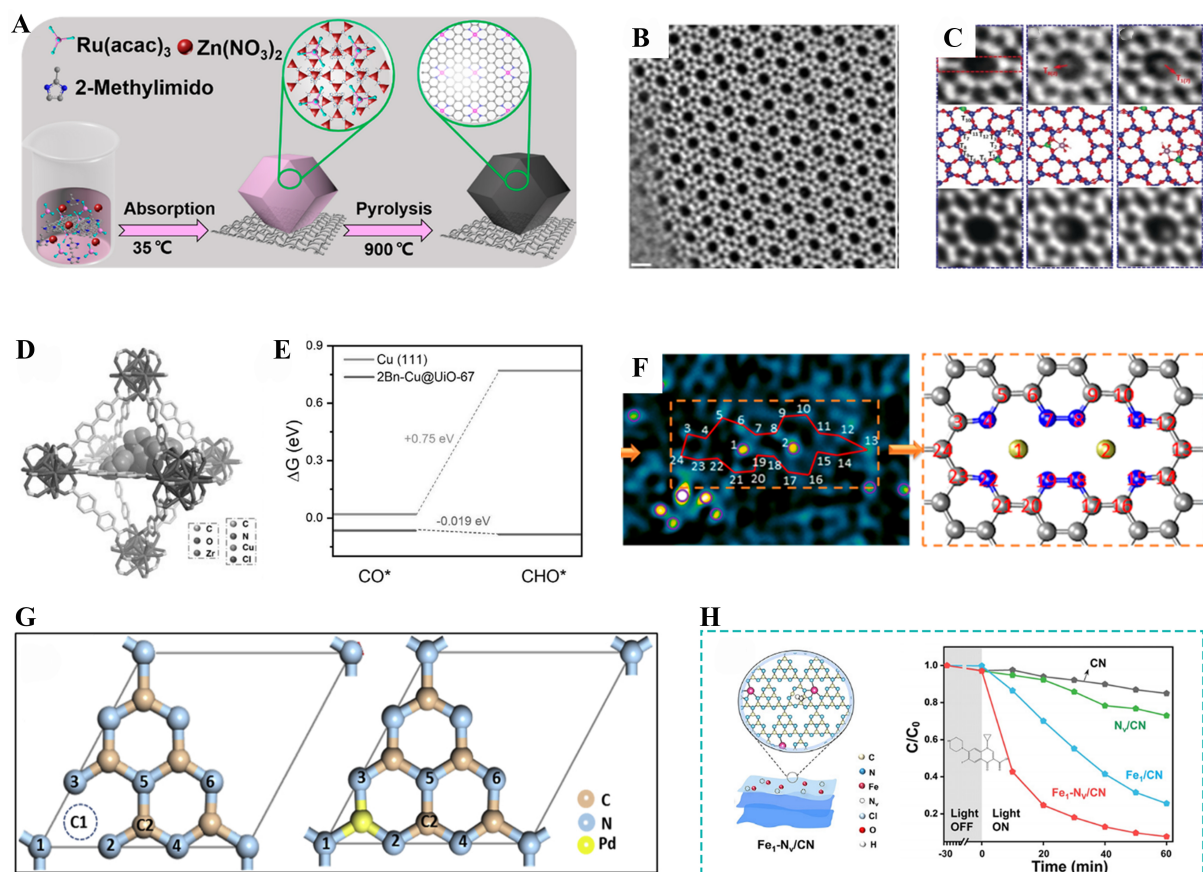


**Figure 10.** (A) Scheme of the formation of Ru SAs confined on NC<sup>[86]</sup>. Copyright 2023, ACS Publications; (B) A representative iDPC-STEM image of Mo/ZSM-5; (C) Zoomed-in three scenarios: empty channel, channels containing a MoO<sub>3</sub>H cluster bound at the T8 site and at the T<sub>1</sub> site<sup>[87]</sup>. Copyright 2023, Wiley; (D) Molecular modeling of 2Bn-Cu@UiO-67; (E) Calculated free-energy diagrams for CO<sub>2</sub> RR over 2Bn-Cu@UiO-67 and Cu (111)<sup>[88]</sup>. Copyright 2023, Wiley; (F) HAADF image of A-CoPt-NC and Model of the configuration of the two metal atoms trapped in the defect<sup>[27]</sup>. Copyright 2023, ACS Publications; (G) Illusion of carbon vacancies sites and Pd single-atom-site in g-C<sub>3</sub>N<sub>4</sub><sup>[89]</sup>. Copyright 2023, Elsevier; (H) Illusion of Fe<sub>1</sub>-N<sub>2</sub>/CN ultrathin nanosheets, and CIP Degradation curves of CN, N<sub>2</sub>/CN and Fe<sub>1</sub>-N<sub>2</sub>/CN<sup>[90]</sup>. Copyright 2023, Wiley. SAs: Single atoms; iDPC-STEM: integrated differential phase-contrast scanning transmission electron microscopy; HAADF: high-angle annular dark field.

## EFFICIENT SINGLE ATOM ELECTROCATALYSTS FOR NRR

SACs have displayed outstanding catalytic activity and selectivity in other electrochemical reactions, including HER<sup>[92-94]</sup>, OER<sup>[95-97]</sup>, ORR<sup>[98,99]</sup>, CO<sub>2</sub>RR<sup>[100,101]</sup>, etc., due to their 100% atomic utilization and strong interactions between active centers and matrices. Thanks to the merits, the SACs were also applied in the NRR and were supposed to adsorb and activate the inert N≡N bonds with high binding energy. Different from the bulk catalysts, the active metal centers in SACs coordinating with supporting atoms are usually partially charged, which substantially accelerate the activation of N<sub>2</sub>. In addition, the uniform active centers can be modified precisely on the atomic scale<sup>[102-104]</sup>.

Generally, the electrochemical NRR process includes three steps: (i) generation and migration of protons (H<sup>+</sup>) in the electrolyte; (ii) adsorption of N<sub>2</sub> on the surface of electrocatalyst; (iii) hydrogenation of N<sub>2</sub> to form NH<sub>3</sub>. DFT calculations verify that the NRR on metal active sites is limited by the linear relation between the adsorption energies of <sup>\*</sup>N<sub>2</sub>H and <sup>\*</sup>NH<sub>2</sub> intermediates. The outstanding NRR catalysts should satisfy the following three standards: (i) the catalysts should be able to bind the N<sub>2</sub> molecule and subsequently activate the N≡N bond; (ii) the active sites should selectively stabilize the <sup>\*</sup>N<sub>2</sub>H intermediate for

suppressing the competitive HER process; (iii) the linear scaling between  $\text{N}_2\text{H}$  and  $\text{NH}_2$  should be broken to destabilize the  $\text{NH}_2$  intermediate for the releasing of  $\text{NH}_3$  molecules<sup>[4,105]</sup>.

On this basis, large amounts of DFT calculation research on SACs were investigated to evaluate the NRR activity on different supports<sup>[106-109]</sup>. For example, Choi *et al.* demonstrated the NRR performance of SACs anchored on defected graphene with various coordination structures, such as  $\text{M@C}_3$ ,  $\text{M@C}_4$ ,  $\text{M@N}_3$ , and  $\text{M@N}_4$ <sup>[108]</sup>. It was investigated that the adsorption of  $\text{H}$  on SACs was inhibited, in comparison with the bulk metal surfaces. The interactions between metal atoms with defected graphene make metal active sites positively charged, enabling metal centers to bind and activate  $\text{N}_2$  more easily. The  $\text{Ti-N}_4$  and  $\text{V-N}_4$  are considered to be optimal configurations as NRR catalysts. Zhao *et al.* studied the NRR catalytic activity over transition metal atoms on boron nitride (BN) monolayers with rich B vacancies<sup>[109]</sup>. The  $\text{N}_2$  adsorption on transition metal (i.e., Ti, V, Mn, Fe, Mo, Ru, and Rh)-doped BN is an exothermic process, indicating energetically favorable adsorption of  $\text{N}_2$  molecules on these active sites. Among all the investigated materials, the Mo-BN catalyst displays the best NRR performance via an enzymatic reaction pathway, requiring quite a low overpotential of 0.19 V. The breakage of linear scaling between the adsorption of  $\text{N}_2\text{H}$  and  $\text{NH}_2$ , along with the high spin-polarization of Mo, contributes to the outstanding performance of the Mo-BN catalyst. Inspired by these DFT calculation results, many researchers have designed and fabricated the SACs for NRR following the predicted structures. Table 1 shows the summary of SACs along with the corresponding materials, metal contents and their performances for NRR.

### Noble metal-based materials

Noble metals have a crucial effect on various electrocatalytic reactions in view of their superior catalytic activity. Researchers have developed a series of Noble metal-based SACs on NRR<sup>[110-113]</sup>. Wang *et al.* synthesized isolated gold single atoms anchored on  $\text{C}_3\text{N}_4$  nanosheets. Thanks to the high atom utilization, a  $\text{NH}_3$  yield rate of  $1,305 \text{ g}\cdot\text{h}^{-1}\cdot\text{mg}_{\text{Au}}^{-1}$  was obtained with a FE of 11.1%, approximately 22.5 times that for Au nanoparticles [Figure 11A-C]<sup>[114]</sup>. To further improve the catalytic activity, Sun *et al.* fabricated the Au SACs in  $\beta\text{-FeOOH}$  with large surface area, yielding a  $2,860 \text{ }\mu\text{g}\cdot\text{h}^{-1}\cdot\text{mg}_{\text{Au}}^{-1}$  at  $-0.4 \text{ V vs. RHE}$ , exceeding lots of reported Au-based NRR catalysts [Figure 11D and E]<sup>[115]</sup>. Experiment results and DFT results reveal that the charge transfer from  $\beta\text{-FeOOH}$  to anchoring Au single atoms further facilitates the injection of electrons to  $\text{N}_2$  for activating the NRR process. The synergistic effect of porous  $\beta\text{-FeOOH}$  and high activity of isolated dispersed Au contributes to the high NRR catalytic activity. Geng *et al.* fabricated Ru single species on NC (Ru SAs/N-C) via calcinating the Ru-containing ZIF-8<sup>[116]</sup>. The  $\text{NH}_3$  yield rate of Ru SAs/N-C reaches at  $120.9 \text{ }\mu\text{g}\cdot\text{mg}_{\text{cat}}^{-1}\cdot\text{h}^{-1}$  at  $-0.2 \text{ V vs. RHE}$  with a FE of 29.6%.

Although the noble-based SACs possess high NRR catalytic activity, they also show excellent HER performance, which results in severe competing HER and leads to low FE. Therefore, introducing another element that inhibits the HER activity is considered as a feasible strategy for adjusting the NRR selectivity. He *et al.* constructed active bimetallic sites via the combination of transition metal heteroatoms (e.g., Fe, Co, Mo, and W) and Ru through the DFT calculation. The energy barriers of the first and last hydrogenation process for bimetallic sites are much lower than those of Ru active sites [Figure 11F-I]<sup>[117]</sup>. The resulting Mo-Ru species displayed an ultra-low onset potential of only 0.17 V [Figure 11G]. They revealed that the side-on adsorption mode and synergistic action of bimetal configuration moderate the adsorption energy of key intermediates and thus suppress HER side reaction. Han *et al.* designed a diatomic Pd-Cu site on NC for modulating the Pd sites with Cu elements<sup>[118]</sup>. It is demonstrated that the introducing of Cu can not only upshift the density states of Pd to the fermi level but also enhance the  $d\text{-}2^*$  orbital hybridization between Pd and  $\text{N}_2$  molecules, leading to the promotion of  $\text{N}_2$  activation and suppressed hydrogen evolution [Figure 11J]. As a result, the PdCu/NC catalyst gives rise to a high FE of  $24.8\% \pm 0.8\%$ , 14.6 times and three times of Pd/NC and Cu/NC, respectively [Figure 11K]. The  $\text{N}^{15}$  isotopic labeling experiment confirmed that

**Table 1. Summary of single atom catalysts for NRR application**

Electrocatalysts	Metal content (%)	Electrolyte	NH <sub>3</sub> yield and FE	Ref.
Au/TiO <sub>2</sub>	1.54 wt% (ICP-MS)	0.1 M HCl	21.4 μg·h <sup>-1</sup> ·mg <sub>cat</sub> <sup>-1</sup> /8.11%	[111]
Ru@ZrO <sub>2</sub> /NC	0.1wt% (ICP-AES)	0.1 M HCl	3.665 μg·h <sup>-1</sup> ·mg <sub>Ru</sub> <sup>-1</sup> /21%	[112]
Au1/C <sub>3</sub> N <sub>4</sub>	0.15% (ICP-OES)	5 M H <sub>2</sub> SO <sub>4</sub>	1,305 μg·h <sup>-1</sup> ·mg <sub>Au</sub> <sup>-1</sup> /11.1%	[114]
Au-SA/FeOOH	2.0 wt%	0.05 M H <sub>2</sub> SO <sub>4</sub>	2.860 μg·h <sup>-1</sup> ·mg <sub>cat</sub> <sup>-1</sup> /14.2%	[115]
Ru SAs/N-C	2.64%	0.05 M H <sub>2</sub> SO <sub>4</sub>	120.9 μg·mg <sub>cat</sub> <sup>-1</sup> ·h <sup>-1</sup> /29.6%	[116]
PdCu/NC	Pd: 2.23 wt% Cu: 2.32 wt% (ICP-AES)	0.05 M H <sub>2</sub> SO <sub>4</sub>	69.2 ± 2.5 μg·h <sup>-1</sup> ·mg <sub>cat</sub> <sup>-1</sup> /24.8% ± 0.8%	[118]
PdFe <sub>1</sub>	Fe: 3.91 at%	0.5 M LiClO <sub>4</sub>	111.9 μg·h <sup>-1</sup> ·mg <sup>-1</sup> /37.8%	[65]
Fe SAC	1.51 wt% (ICP-OES)	0.5 M KNO <sub>3</sub> + 0.1 M K <sub>2</sub> SO <sub>4</sub>	0.46 mmol·h <sup>-1</sup> ·cm <sup>-2</sup> /75%	[5]
Fe-PPy SACs	2.38 wt% (ICP-MS)	0.1 M KOH + 0.1 M KNO <sub>3</sub>	2.75 mg·h <sup>-1</sup> ·cm <sup>-1</sup>	[105]
Fe <sub>1</sub> -N-C	1.71 wt% (ICP-AES)	0.1 M HCl	1.56 × 10 <sup>-11</sup> mol·cm <sup>-2</sup> ·s <sup>-1</sup> /4.51%	[123]
ISAS-Fe/NC	4.2 wt% (ICP-AES)	0.1 M PBS	62.9 ± 2.7 μg·h <sup>-1</sup> ·mg <sub>cat</sub> <sup>-1</sup> /18.6% ± 0.8%	[125]
FeSA-N-C	1.09 wt% (ICP-AES)	0.1M KOH	7.48 μg·h <sup>-1</sup> ·mg <sup>-1</sup> /56.55%	[126]
Fe-SAs/LCC	0.60 wt% (ICP-AES)	0.1M KOH	5,350 μg·h <sup>-1</sup> ·mg <sub>Fe</sub> <sup>-1</sup> /29.3%	[127]
Fe-MoS <sub>2</sub>	2.0 wt%	0.1 M KCl	36.1 ± 3.6 mmol·g <sup>-1</sup> ·h <sup>-1</sup> /31.6% ± 2%	[131]
Fe-MoS <sub>2</sub>	5.3 at% (ICP-AES)	0.5 M K <sub>2</sub> SO <sub>4</sub> (pH = 3)	8.63 μg·h <sup>-1</sup> ·mg <sub>cat</sub> <sup>-1</sup> /18.8%	[132]
SA-Mo <sub>2</sub> /NPC	9.54% (ICP-AES)	0.1M KOH	34.0 ± 3.6 μg·h <sup>-1</sup> ·mg <sub>cat</sub> <sup>-1</sup> /14.6% ± 1.6%	[134]
B-Mo <sub>2</sub> C/NC-50	-	0.5 M K <sub>2</sub> SO <sub>4</sub>	52.1 μg·h <sup>-1</sup> ·mg <sup>-1</sup> /36.9%	[135]
Ni-Mo <sub>2</sub> C/NC	-	0.5 M K <sub>2</sub> SO <sub>4</sub>	46.49 μg·h <sup>-1</sup> ·mg <sup>-1</sup> /29.05%	[136]
MoSAs-Mo <sub>2</sub> C/ NCNTs	-	0.005 M H <sub>2</sub> SO <sub>4</sub> and 0.1 M K <sub>2</sub> SO <sub>4</sub>	16.1 μg·h <sup>-1</sup> ·cm <sub>cat</sub> <sup>-2</sup> /7.1%	[137]
Mo/BCN	1.50 wt% (ICP-AES)	0.1M KOH	37.67 μg·h <sup>-1</sup> ·mg <sub>cat</sub> <sup>-1</sup> /13.27%	[140]
Mo/HNG	2.4 wt%	0.05 M H <sub>2</sub> SO <sub>4</sub>	3.6 μg·h <sup>-1</sup> ·mg <sub>cat</sub> <sup>-1</sup> /50.2%	[141]
Mn-O <sub>3</sub> N <sub>1</sub> /PC	3.85 wt% (ICP-AES)	0.1 M HCl	66.41 ± 4.05 μg·h <sup>-1</sup> ·mg <sub>cat</sub> <sup>-1</sup> / 4.91% ± 0.82%	[143]
NC-Cu SA	5.31 wt % (ICP-MS)	0.1 M KOH 0.1 M HCl	-53.3 μg <sub>NH<sub>3</sub></sub> ·h <sup>-1</sup> ·mg <sub>cat</sub> <sup>-1</sup> /13.8% -49.3 μg <sub>NH<sub>3</sub></sub> ·h <sup>-1</sup> ·mg <sub>cat</sub> <sup>-1</sup> /11.7%	[144]
Y <sub>1</sub> /NC; Sc <sub>1</sub> /NC	-	0.1 M HCl	23.2 μg·cm <sup>-2</sup> ·h <sup>-1</sup> /12.1% 20.4 μg·cm <sup>-2</sup> ·h <sup>-1</sup> /11.2%	[146]

NRR: Nitrogen reduction reaction; FE: Faradic efficiency; NC: N-doped carbon; SA: single atom; SAC: single atom electrocatalyst; PPy: polypyrrole; PBS: phosphate buffer saline; NPC: nitrogen doped porous carbon; NCNTs: N-doped carbon nanotubes; Mo/BCN: B and N co-doped Mo SACs.

ammonia was produced from the NRR process [Figure 11L].

### Non-noble metal-based SACs

Non-noble metals, especially transition metal-based SACs, are considered as the alternative of noble materials in view of their cost effectiveness, resource abundance, and comparable catalytic activity to noble metals. Recently, various transition metal-based SACs have been reported as efficient NRR catalysts under ambient conditions.

#### Fe-based SACs

The volcano-type relationship between the nitrogen adsorption energy and the NRR catalytic activity of different metals identified that the non-noble metals (Mo, Fe) that on the top of volcano diagrams are the most active metals. The viability of atomical Fe-based catalysts in the NRR field has been confirmed by theoretical studies<sup>[79,119-121]</sup>. For instance, DFT calculation results indicate that the outstanding NRR performance of FeN<sub>3</sub> species on graphene was assigned to the high-spin polarization of FeN<sub>3</sub> configuration<sup>[122]</sup>. Based on this, numerous atomically dispersed Fe SACs have been developed for

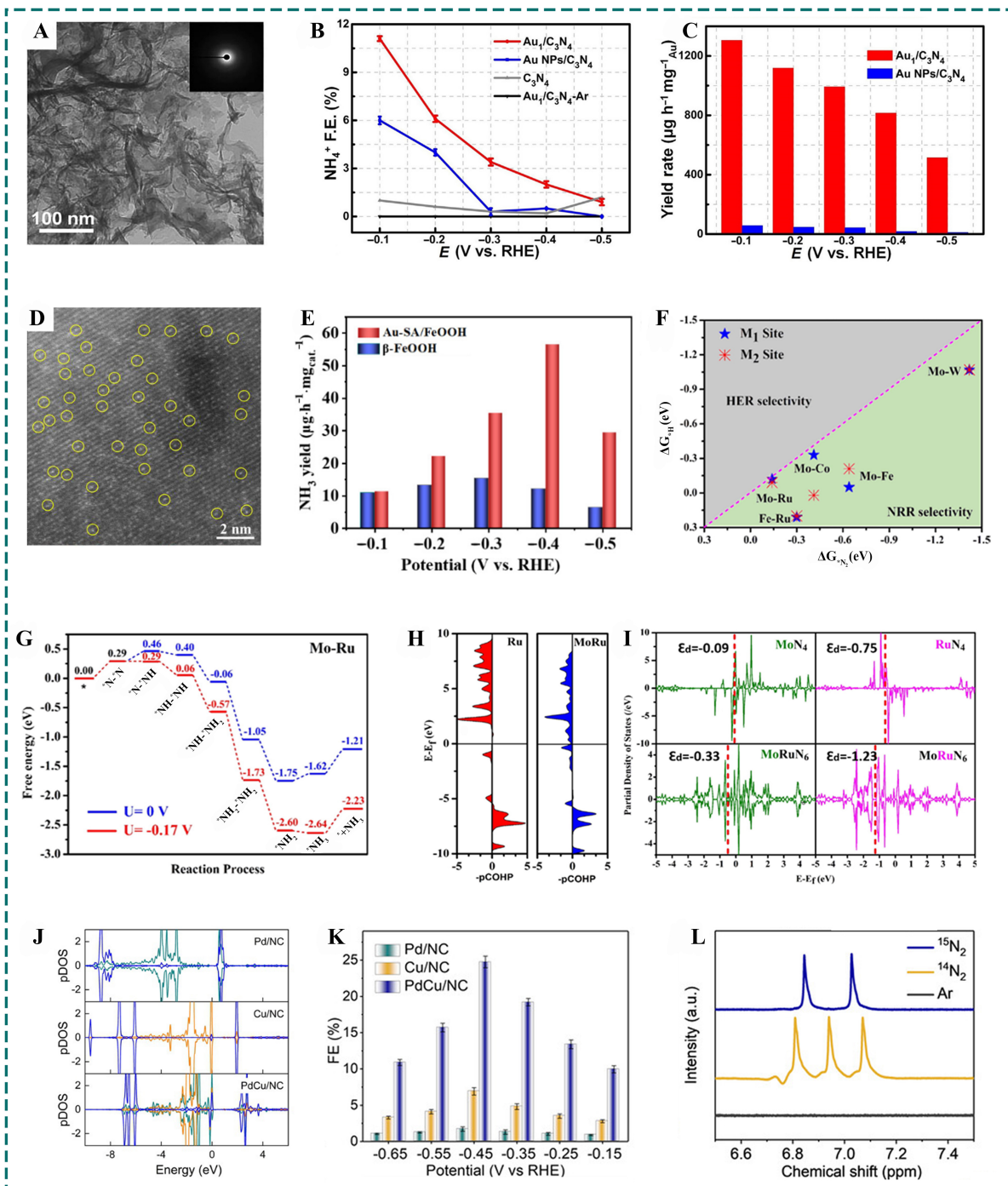


**Figure 11.** (A) TEM observation of  $\text{Au}_1/\text{C}_3\text{N}_4$ ; (B)  $\text{NH}_4^+$  formation Faradaic efficiencies for  $\text{Au}_1/\text{C}_3\text{N}_4$ ,  $\text{Au NPs}/\text{C}_3\text{N}_4$ , pure  $\text{C}_3\text{N}_4$  and  $\text{Au}_1/\text{C}_3\text{N}_4\text{-Ar}$ ; (C)  $\text{NH}_4^+$  yield rates normalized by Au mass<sup>[114]</sup>. Copyright 2023, Elsevier; (D) HAADF-STEM images of  $\text{Au-SA}/\text{FeOOH}$ ; (E)  $\text{NH}_3$  yields for  $\text{Au-SA}/\text{FeOOH}$  and  $\beta\text{-FeOOH}$ <sup>[115]</sup>. Copyright 2023, Springer Nature; (F) The free energy for H and  $\text{N}_2$  adsorption on these five selected candidates; (G) The calculated free energy profiles for NRR through enzymatic mechanism on  $\text{Mo-Ru}$ ; (H) Projected crystal orbitals and (I) d-band centers of Ru and  $\text{Mo-Ru}$  dual-site<sup>[117]</sup>. Copyright 2023, Elsevier; (J) Computed electronic properties and (K) FE for  $\text{Pd}/\text{NC}$ ,  $\text{Cu}/\text{NC}$ , and  $\text{PdCu}/\text{NC}$ ; (L)  $^1\text{H}$  spectra of electrolyte after 2 h of electrochemical reduction on  $\text{PdCu}/\text{NC}$  using  $\text{Ar}$ ,  $^{14}\text{N}_2$  and  $^{15}\text{N}_2$  as the feeding gases. TEM: Transmission electron microscopy; HAADF-STEM: high-angle annular dark field scanning transmission electron microscopy; NRR: nitrogen reduction reaction; FE: Faradaic efficiency.

NRR<sup>[19,105,123,124]</sup>. Lü *et al.* dispersed Fe active sites in Fe-N<sub>4</sub> configuration on NC via calculating the Fe-doped ZIF-8 [Figure 12A]<sup>[125]</sup>. Figure 12B shows the NRR performance of Fe-N<sub>4</sub>, which achieves a NH<sub>3</sub> yield rate (62.9 μg·h<sup>-1</sup>·mg<sub>cat</sub><sup>-1</sup>) and high FE (18.6%) in 0.1 M phosphate buffer saline (PBS) electrolyte. Long catalytic stability of the Fe/NC catalyst was revealed by electrolyzing for 24 h with negligible activity decay. Wang *et al.* immobilized Fe sites by modulation of the PPy-iron coordination complex to achieve a high FE of 56.55% in 0.1 M KOH solution [Figure 12C and D]<sup>[126]</sup>. Zhang *et al.* reported Fe-SAC catalyst with Fe-(O-C<sub>2</sub>)<sub>4</sub> coordination configuration for the first time<sup>[127]</sup>. The lignocellulose (LC) with abundant oxygen functional groups was employed as a precursor to obtain carbon support for anchoring Fe sites [Figure 12E]. This unit Fe-(O-C<sub>2</sub>)<sub>4</sub> active sites yield a high NH<sub>3</sub> rate of 5,350 μg·h<sup>-1</sup>·mg<sub>Fe</sub><sup>-1</sup> [Figure 12F].

Immobilizing Fe atoms on other transition metal compounds or alloys to regulate the band structure of Fe species through neighboring metal-support interaction is also beneficial for improving NRR performance<sup>[73,119,123,128-130]</sup>. Li *et al.* immobilized the protrusion-shaped Fe atoms on MoS<sub>2</sub> [Figure 12G-I]<sup>[131]</sup>. The engendered polarization electric field accelerates the electron transfer into antibonding orbitals of N<sub>2</sub> for adsorbing and activating N<sub>2</sub> molecules. Moreover, this strategy was also extended to other metals, such as Co-MoS<sub>2</sub>, Cu-MoS<sub>2</sub>, Rh-MoS<sub>2</sub>, and Ru-MoS<sub>2</sub>. Su *et al.* also confirmed that coordination of Fe species with edge S sites of MoS<sub>2</sub> is beneficial for suppressing the competing HER, with the FE of Fe-MoS<sub>2</sub> six times larger than that of MoS<sub>2</sub><sup>[132]</sup>. Li *et al.* stabilized isolated Fe active sites with Pd nanosheets to generate PdFe<sub>x</sub> SAAs<sup>[79]</sup>. In this unique architecture, the Fe atoms not only act as the active sites to adsorb N<sub>2</sub> molecules but also ensure a good balance between the N<sub>2</sub> activation and nitrogen intermediate stabilization. Nevertheless, the Fe multimers bind too strongly with the intermediates and thus result in compromised NRR activity [Figure 12J]. As a result, 111.9 μg·h<sup>-1</sup>·mg<sup>-1</sup> of ammonia yield and 37.8% of FE was obtained at -0.2 V vs. RHE, which is 7.1 and 2.4 times higher than that of Pd and PdFe<sub>x</sub> [Figure 12K and L].

#### Mo-based SACs

It is well known that nearly all natural N<sub>2</sub> is fixed with the enzyme nitrogenase in bacteria, and the Mo elements act as the main active sites. Therefore, Mo-based materials (especially Mo SACs) have been considered as the most promising catalysts for NRR. Ling *et al.* first revealed by the DFT calculation that Mo<sub>1</sub>-N<sub>1</sub>C<sub>2</sub> possesses expected NRR catalytic activity with an enzymatic mechanism and can release NH<sub>3</sub> molecules with a low energy barrier, exceeding most ever reported NRR catalysts<sup>[133]</sup>. Inspired by this, Han *et al.* immobilized the Mo single species with nitrogen doped porous carbon (NPC) with a mass loading of 9.54% to catalyze the NRR and yielded a NH<sub>3</sub> rate of 34.0 μg·h<sup>-1</sup>·mg<sub>cat</sub><sup>-1</sup> with a high FE of 14.6% [Figure 13A and B]<sup>[134]</sup>. Previous research reported that Mo<sub>2</sub>C possessing abundant unoccupied *d* orbitals also delivers effective N<sub>2</sub> adsorption capability<sup>[135,136]</sup>. Therefore, Ma *et al.* combined atomically Mo and Mo<sub>2</sub>C on NC nanotubes to prepare the MoSAs-Mo<sub>2</sub>C/NCNTs catalyst [Figure 13C]. In this structure, Mo<sub>2</sub>C is selective to NRR, while the HER selective Mo SAs enable the increase of \*H coverage near the Mo<sub>2</sub>C nanoparticles [Figure 13D and E]. The synergistic mechanism of Mo SAs and Mo<sub>2</sub>C makes the NH<sub>3</sub> catalytic activity of MoSAs-Mo<sub>2</sub>C/NCNTs catalyst four times and 4.5 times higher than that of Mo<sub>2</sub>C nanoparticles and Mo SAs, respectively<sup>[137]</sup>. Wang *et al.* also demonstrated that the positively charged isolated Mo species produced by denoting electrons to PC-TFPN substrate has low binding affinity to H, which is conducive to suppress the competing HER [Figure 13F]<sup>[138]</sup>. Chen *et al.* also proved that the Mo-N<sub>3</sub>C activity sites with positive charge have higher NRR catalytic activity than Mo-N<sub>0</sub>C, Mo-N<sub>1</sub>C, and Mo-N<sub>2</sub>C<sup>[139]</sup>. In addition, B and N co-doped Mo SACs (Mo/BCN) have been designed and fabricated by Shi *et al.* for catalyzing NRR in 0.1 alkaline electrolyte. EXAFS result verifies the four-coordination structure of Mo single sites with two N atoms and two B atoms to form MoB<sub>2</sub>N<sub>2</sub> active sites [Figure 13G], which activated the N<sub>2</sub> molecules in the first hydrogenation process via a distal mechanism. The Mo/BCN catalyst obtains a high FE of 13.27%<sup>[140]</sup>. Zhang *et al.* stabilized atomical Mo on graphene layers with abundant holes through a facile potassium sat-

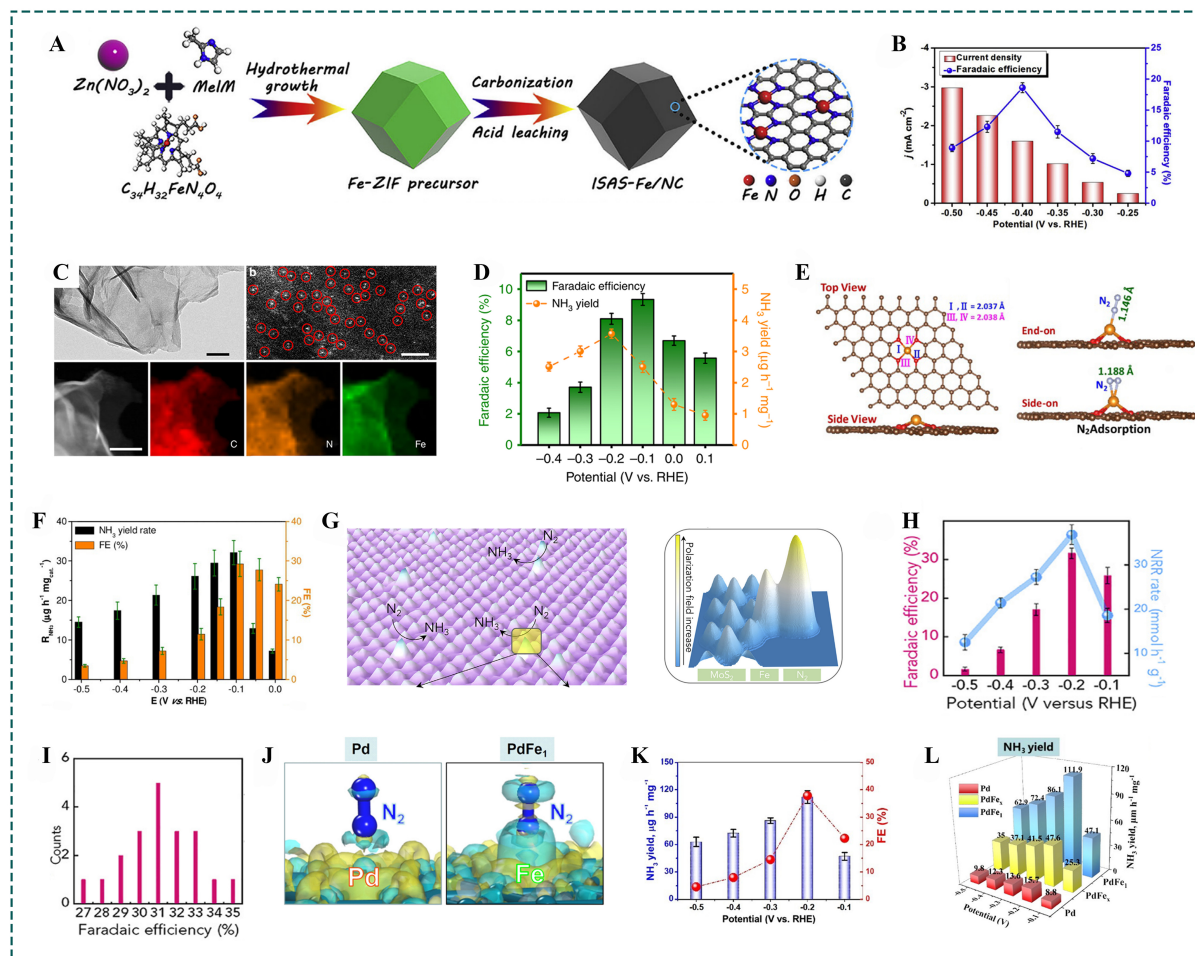


**Figure 12.** (A) Illustration of ISAS-Fe/NC catalyst synthesis; (B) Average  $j$  and FEs measured in  $N_2$ -saturated 0.1 M PBS solution<sup>[125]</sup>. Copyright 2023, Elsevier; (C) TEM image, HAADF-STEM image and corresponding EDS mapping images of single-atom dispersed Fe-N-C; (D)  $NH_3$  yield rate and FE of Fe-N-C catalysts<sup>[126]</sup>. Copyright 2023, Springer Nature; (E) Optimized Fe-(O-C<sub>2</sub>)<sub>4</sub> sites and  $N_2$  adsorption on Fe-(O-C<sub>2</sub>)<sub>4</sub>; (F) Dependence of  $R_{NH_3}$  and FE on the applied potentials<sup>[127]</sup>. Copyright 2023, Wiley; (G) Polarization fields formed between Fe atoms and MoS<sub>2</sub> boost the  $N_2$  activation; (H) and (I)  $NH_3$  yield rate and FE of Fe-MoS<sub>2</sub> catalysts<sup>[131]</sup>. Copyright 2023, Elsevier; (J) Different charge densities of  $N_2$  adsorbed on Pd and PdFe; (K)  $NH_3$  yield rate and FE of PdFe<sub>x</sub> catalysts; (L) The comparison of  $NH_3$  yield rate of Pd, PdFe<sub>x</sub> and PdFe<sub>x</sub><sup>[79]</sup>. Copyright 2023, Wiley. FE: Faradic efficiency; PBS: phosphate buffer saline; TEM: transmission electron microscopy; HAADF-STEM: high-angle annular dark field scanning transmission electron microscopy.

assisted activation method [Figure 13H-J]. DFT results unveil that the edge-coordinated Mo sites combined with the vacancies on the hole graphene could effectively lower the reaction energy barrier of the NRR process compared to the original perfect graphene. As a result, an exceptional FE of 50.2% was yielded at -0.05 V vs. RHE [Figure 13K]<sup>[141]</sup>.

#### Other transition metal-based SACs

Besides above-mentioned widely studied Fe and Mo atomically catalysts, other transition metal-based SACs, containing Ni, Mn, W, Co, etc., were also investigated. Atomical Ni active site coordinated with nitrogen environment was produced by Mukherjee *et al.*, delivering a  $NH_3$  yield of 115  $\mu\text{g}\cdot\text{cm}^{-2}\cdot\text{h}^{-1}$  at -0.8 V vs. RHE with a high FE of 21% [Figure 14A]. DFT results reveal that the NiN<sub>3</sub>, as the main active sites, can catalyze NRR process completely thermodynamically favorably under a limiting potential of 0.79 V<sup>[142]</sup>. In addition, black phosphorene (BP) was also employed as the substrate to immobilize the transition metal atoms with

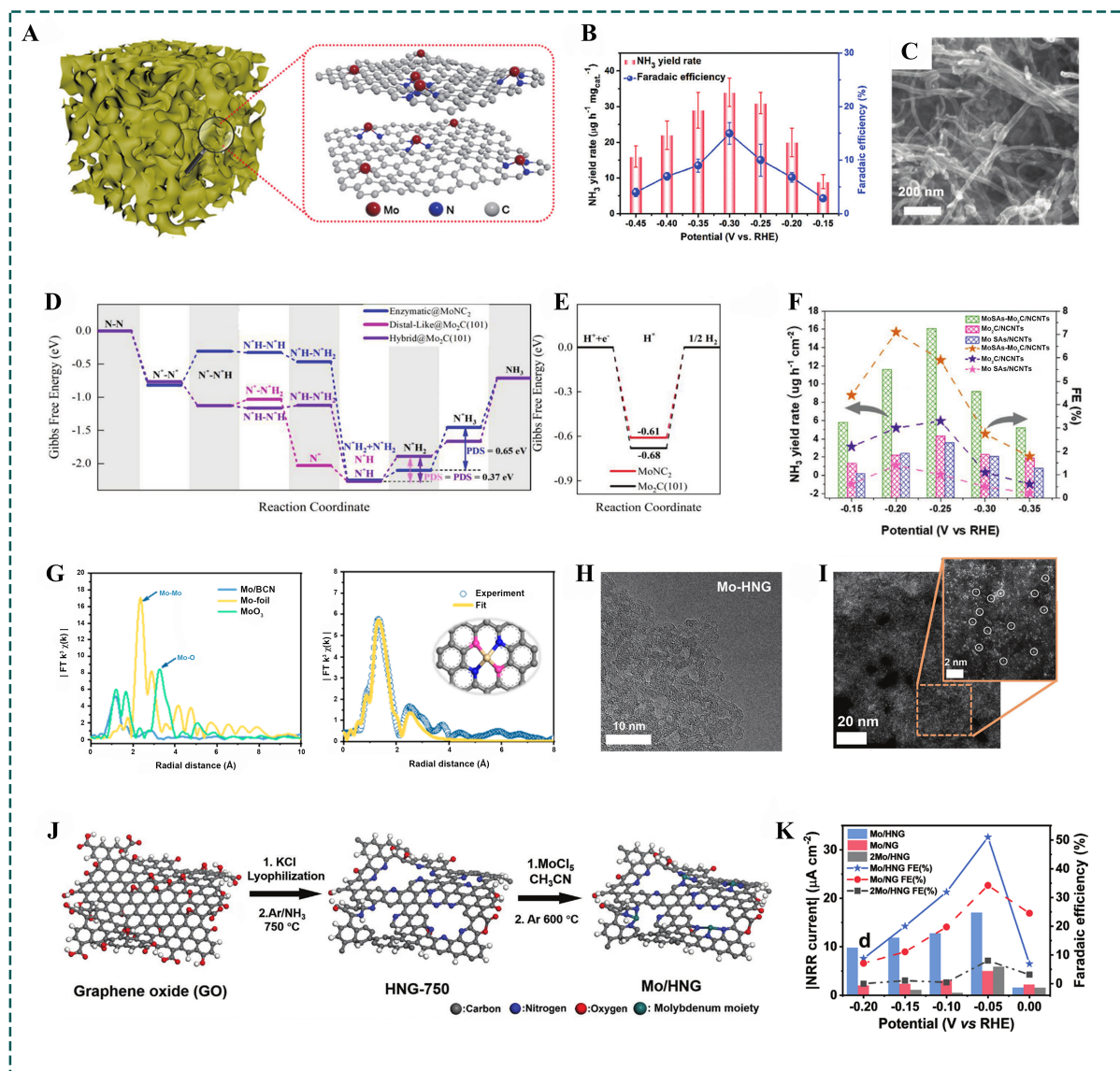


**Figure 13.** (A) Illustration of SA-Mo/NPC and atomic structure model; (B)  $\text{NH}_3$  yield rate (red) and FE (blue) at each given potential of SA-Mo/NPC<sup>[134]</sup>. Copyright 2023, Wiley; (C) SEM image of MoSAs-Mo<sub>2</sub>C/NCNTs; The (D) NRR and (E) HER Gibbs free energy diagrams on the MoNC<sub>2</sub> SAC and Mo<sub>2</sub>C (101) surface; (F)  $\text{NH}_3$  yield rate and FE of MoSAs-Mo<sub>2</sub>C/NCNTs, MoSAs/NCNTs and Mo<sub>2</sub>C/NCNTs<sup>[137]</sup>. Copyright 2023, Wiley; (G) FT of the EXAFS spectra at the k3-weighted Kedges and fitting of FT EXAFS spectra of Mo/BCN<sup>[140]</sup>. Copyright 2023, ACS Publications; (H) HRTEM images of the Mo-HNG catalyst; (I) HAADF-STEM images of Mo-HNG and magnified area with circled individual Mo atoms immobilized on the carbon matrix presumably at N-rich edges; (J) Synthesis and morphological characterization of the Mo/HNG catalyst and (K) Potential dependent FEs and partial current densities of  $\text{NH}_3$  for NRR on Mo/HNG, Mo/NG, 2Mo/HNG catalysts<sup>[141]</sup>. Copyright 2023, Wiley. SA: Single atom; NPC: nitrogen doped porous carbon; FE: Faradaic efficiency; SEM: scanning electron microscopy; NCNTs: N-doped carbon nanotubes; NRR: nitrogen reduction reaction; HER: hydrogen evolution reaction; SAC: single atom electrocatalyst; EXAFS: extended X-ray absorption fine structure; Mo/BCN: B and N co-doped Mo SACs; HAADF-STEM: high-angle annular dark field scanning transmission electron microscopy.

$\text{MP}_3$  coordinated structure (M = Fe, Mn, Cr, Mo, W, V, and Nb). Among these catalysts, W@BP delivers the highest NRR activity and selectivity, which is ascribed to the unique  $\text{WP}_3$  active sites that activate the  $\text{N}\equiv\text{N}$  bonds by injecting electrons to  $\text{N}_2$ , thereby regulating the electron transfer between BP and nitrogen containing intermediates [Figure 14B and C]<sup>[124]</sup>. Han *et al.* constructed Mn-O<sub>3</sub>N<sub>1</sub> active sites on P-doped porous carbon through the local modulation of Mo-O bonding conditions [Figure 14D and E]<sup>[143]</sup>. In this

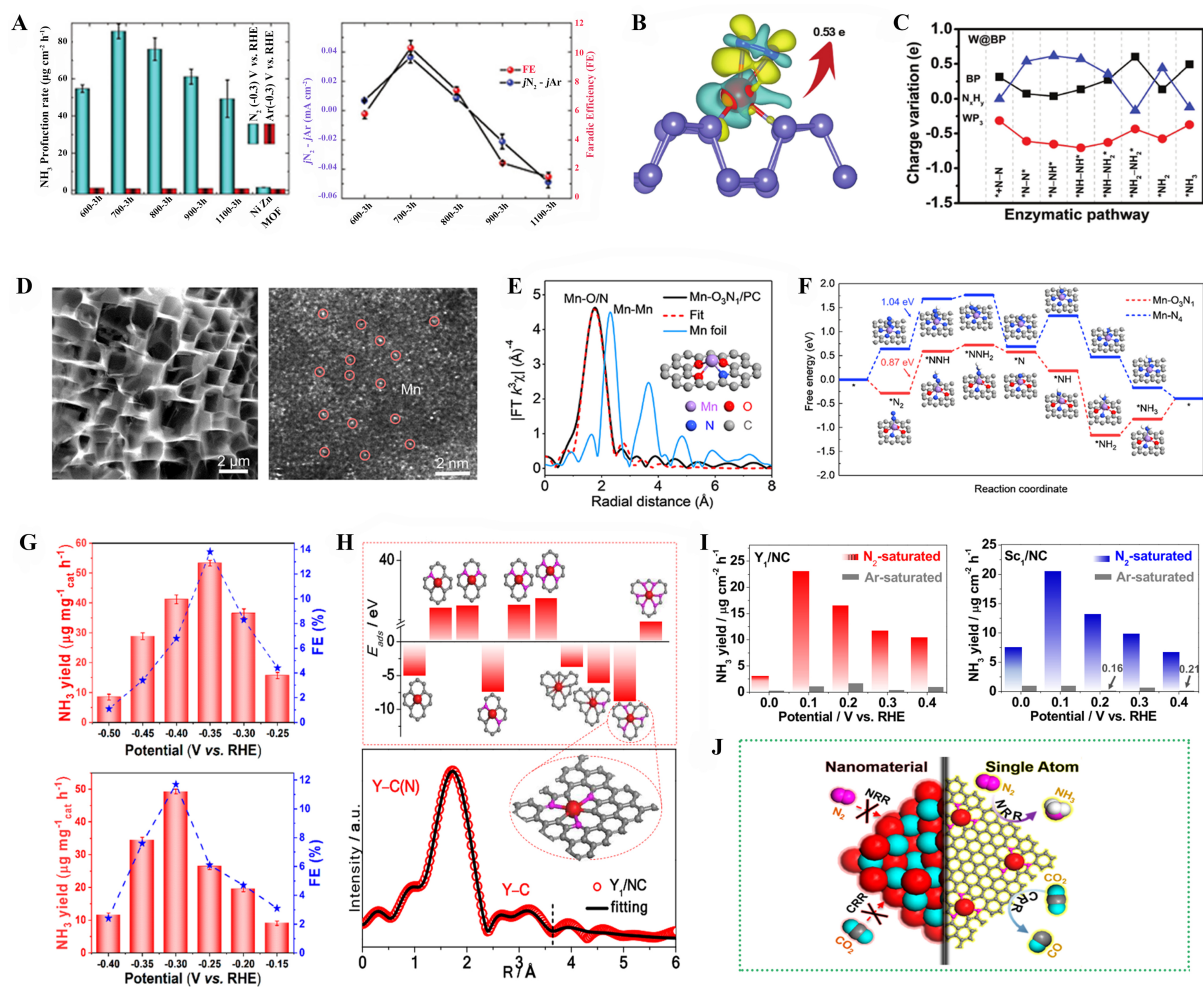


**Figure 14.** (A) Comparison of  $\text{NH}_3$  production rate and FE at different pyrolysis in 0.1 M KOH solution<sup>[142]</sup>. Copyright 2023, Wiley; (B) Charge density difference between W@BP and  $\text{N}_2$  with side-on configurations; (C) The reaction pathways on W-BP<sup>[124]</sup>. Copyright 2023, RSC Publishing; (D) TEM image and HAADF-STEM image of  $\text{Mn-O}_3\text{N}_1/\text{PC}$ ; (E) FT-EXAFS spectra of Mn foil,  $\text{Mn-O}_3\text{N}_1/\text{PC}$ , and the curve fitting with the  $\text{Mn-O}_3\text{N}_1/\text{graphene}$ ; (F) Free energy diagram of an associative distal pathway on the  $\text{Mn-O}_3\text{N}_1/\text{graphene}$  and the  $\text{Mn-N}_4/\text{graphene}$ <sup>[143]</sup>. Copyright 2023, ACS Publication; (G) The  $\text{NH}_3$  yield rate and FE at different potentials in 0.1 M KOH and 0.1 M HCl<sup>[144]</sup>. Copyright 2023, ACS Publication; (H) Calculated active site structures of an yttrium single atom and corresponding adsorption energies and FT-EXAFS fitting in R-space of  $\text{Y}_1/\text{NC}$ ; (I) The  $\text{NH}_3$  yield rate and FE of  $\text{Y}_1/\text{NC}$ ; (J) The NRR catalytic activity of Y/Sc based nanomaterials and single atom catalysts<sup>[146]</sup>. Copyright 2023, ACS Publication. FE: Faradic efficiency; TEM: transmission electron microscopy; HAADF-STEM: high-angle annular dark field scanning transmission electron microscopy; EXAFS: extended X-ray absorption fine structure; NRR: nitrogen reduction reaction.

structure, the more electronegativity of O prompts more electrons transfer from Mo to O, making Mn sites more active than  $\text{MnN}_4$  in the  $\text{N}_2$  adsorption process ( $\Delta E_{\text{N}_2}$  is -0.83 V for  $\text{Mn-O}_3\text{N}_1$  and 0.09 V for  $\text{MnN}_4$ ) [Figure 14F]. As a consequence, the  $\text{Mn-O}_3\text{N}_1/\text{PC}$  achieves a  $\text{NH}_3$  yield rate of  $66.41 \mu\text{g}\cdot\text{h}^{-1}\cdot\text{mg}_{\text{cat}}^{-1}$  ( $1.56 \text{ mg}\cdot\text{h}^{-1}\cdot\text{mg}_{\text{Mn}}^{-1}$ ). Zang *et al.* developed Cu SACs on  $\text{C}_3\text{N}_4$  nanosheets, which exhibit  $\text{NH}_3$  yield rate and FE of  $\sim 53.3 \mu\text{g}_{\text{NH}_3}\cdot\text{h}^{-1}\cdot\text{mg}_{\text{cat}}^{-1}$  and 13.8% under 0.1 M KOH,  $\sim 49.3 \mu\text{g}_{\text{NH}_3}\cdot\text{h}^{-1}\cdot\text{mg}_{\text{cat}}^{-1}$  and 11.7% under 0.1 M HCl [Figure 14G]. DFT results demonstrated that Cu- $\text{N}_2$  active sites make a major contribution to catalyzing the NRR process via an alternating reaction pathway<sup>[144]</sup>. Zhang *et al.* also immobilized Co single atoms on  $\text{C}_3\text{N}_4$  ( $\text{Co}@-\text{C}_3\text{N}_4$ ) to reveal their NRR catalytic activity, which possess a negative Fermi level and a high energy level of *d*-band position<sup>[145]</sup>. Moreover, yttrium and scandium rare earth SACs were also synthesized on a carbon support ( $\text{Y}_1/\text{NC}$  and  $\text{Sc}_1/\text{NC}$ ) by Liu *et al.*<sup>[146]</sup>. Compared to generally transition metal atoms, the

large size of Sc and Y atoms make them easily stabilized on large carbon defects via a six-coordination structure [Figure 14H]. Y<sub>1</sub>/NC and Sc<sub>1</sub>/NC SACs can effectively catalyze NRR by delivering a NH<sub>3</sub> yield rate of 23.2 and 20.4 μg·cm<sup>-2</sup>·h<sup>-1</sup>, respectively [Figure 14I]. Nevertheless, Y- and Sc-based nanomaterials are generally inert to the electrochemical reactions under ambient conditions [Figure 14J]. This result confirms that regulating microenvironment structure of Y/Sc via the atomic size effect is a feasible and efficient strategy to modulate the intrinsic activity of catalysts.

## CONCLUSION AND PERSPECTIVE

The production of NH<sub>3</sub> at ambient conditions has attracted great interest, but it remains challenging. The rational design of efficient and cost-effective catalysts possessing high catalytic activity and selectivity is the key to realizing an effective NRR process. SACs have gained significant breakthroughs in various electrocatalytic reactions in view of their unique size effect, regulated coordination environment, and electronic structure. In this review, we first summarize the synthesis strategy toward SACs, such as high temperature pyrolysis, MOF derived SACs, impregnation and coprecipitation strategy, SAAs, electrochemical deposition, ALD method, and so on. Then, we highlighted the in-depth theoretical analysis for rationally designing SACs from the following four aspects: coordination components, coordination number of active sites, metal-support interaction and spatial microenvironment regulation. Finally, some previously reported SACs for NRR, such as noble-metal SACs and non-noble transition metals (Fe SACs, Mo SACs, and other metal SACs), and the corresponding mechanisms are presented and demonstrated. Catalysts with atomic level active sites have displayed excellent catalytic activity, selectivity, and electrochemical stability for NRR. However, some challenges in the following aspects still should be addressed for achieving the practical applications for SACs toward NRR:

(i) The SACs with high atomic metal mass loading are still a challenge. As shown in Table 1, the amounts of metal loading in most of the SACs are still low (< 5 wt%). Therefore, exploring feasible synthesis strategies and selecting suitable supports are vital to realizing the improvement of metal active site density and high performance NRR catalytic reaction. Preparing 2D materials with large surface area and introducing defects or vacancies to anchor the metal sites are beneficial for increasing the metal sites amounts in SACs.

(ii) Most previously reported transitional-based SACs only have a promotion in either ammonia yield rate or FE, while another parameter is still unsatisfactory. Especially, the FE for most SACs is smaller than 30%, resulting from the competition HER. However, commercial catalysts usually require comprehensive optimized performance, especially high catalytic activity and selectivity. Therefore, NRR performance of SACs should still be improved for satisfying the commercial applications.

(iii) Stability of the catalyst is also an important indicator to measure whether it can be realized in commercial applications. Generally, the isolated metal active sites are usually stabilized on various supports by the heteroatoms, including N, O, S, P, and so on. However, the heterogeneous species may undergo the degradation during the catalytic reaction process, resulting in the band structure and coordination environment changes of metal species. This leads to an uncontrollable reaction pathway. Therefore, more advanced in situ characterization instruments and DFT calculations should be carried out to unveil the structural evolution of catalysts when catalyzing and thereby clarify the reaction mechanism and stability of designed catalysts. Moreover, the N elements in the N containing catalysts are also critical issues that influence the measurement of the NH<sub>3</sub> yield rate. As a result, the fabrication of N-free SACs is urgently required.

(iv) Up to now, many theoretical computational models have been constructed to study their NRR catalytic activity, some of which have also been verified by the spectroscopies experimentally. Simultaneously, the experiment results reversely promote the new theories to clarify the reaction mechanism. However, the theoretical calculations are usually based on the ideal assumptive models with simplification and tunable parameters. It is essential to match the theoretical results with experimental data for avoiding obtaining the biased conclusions that misguide the research directions. It is believed that the feedback loop between theoretical studies and experimental results may not only effectively guide the rational design of SACs but also unveil the reaction mechanism and kinetics of active centers.

## DECLARATIONS

### Authors' contributions

Drafted the manuscript: Fan B, Yuan H

Participated in the writing and literature discussion: Wang W, Liu Z, Guo J, Yuan H, Tan Y

Coordinated the writing and finalized the manuscript: Fan B, Tan Y

### Availability of data and materials

The data that support the findings of this study are available from the corresponding author upon reasonable request.

### Financial support and sponsorship

This work was supported by the National Natural Science Foundation of China (No. 52072193 and 52101182).

### Conflicts of interest

All authors declared that there are no conflicts of interest.

### Ethical approval and consent to participate

Not applicable.

### Consent for publication

Not applicable.

### Copyright

© The Author(s) 2024.

## REFERENCES

1. Foster SL, Bakovic SIP, Duda RD, et al. Catalysts for nitrogen reduction to ammonia. *Nat Catal* 2018;1:490-500. [DOI](#)
2. Shi L, Yin Y, Wang S, Sun H. Rational catalyst design for N<sub>2</sub> reduction under ambient conditions: strategies toward enhanced conversion efficiency. *ACS Catal* 2020;10:6870-99. [DOI](#)
3. Deng J, Iñiguez JA, Liu C. Electrocatalytic nitrogen reduction at low temperature. *Joule* 2018;2:846-56. [DOI](#)
4. Wan Y, Xu J, Lv R. Heterogeneous electrocatalysts design for nitrogen reduction reaction under ambient conditions. *Mater Today* 2019;27:69-90. [DOI](#)
5. Montoya JH, Tsai C, Vojvodic A, Nørskov JK. The challenge of electrochemical ammonia synthesis: a new perspective on the role of nitrogen scaling relations. *ChemSusChem* 2015;8:2180-6. [DOI](#) [PubMed](#)
6. Wang Y, Su H, He Y, et al. Advanced electrocatalysts with single-metal-atom active sites. *Chem Rev* 2020;120:12217-314. [DOI](#)
7. Qiao B, Wang A, Yang X, et al. Single-atom catalysis of CO oxidation using Pt<sub>1</sub>/FeO<sub>x</sub>. *Nat Chem* 2011;3:634-41. [DOI](#)
8. Zhang J, Liu C, Zhang B. Insights into single-atom metal-support interactions in electrocatalytic water splitting. *Small Methods* 2019;3:1800481. [DOI](#)
9. Song Z, Zhang L, Doyle-Davis K, Fu X, Luo J, Sun X. Recent advances in MOF-derived single atom catalysts for electrochemical applications. *Adv Energy Mater* 2020;10:2001561. [DOI](#)
10. Yu H, Wang Z, Tian W, et al. Boosting electrochemical nitrogen fixation by mesoporous Rh film with boron and sulfur co-doping.

- Mater Today Energy* 2021;20:100681. DOI
11. Cai L, Zhang N, Qiu B, Chai Y. Computational design of transition metal single-atom electrocatalysts on PtS<sub>2</sub> for efficient nitrogen reduction. *ACS Appl Mater Interfaces* 2020;12:20448-55. DOI PubMed
  12. van der Ham CJ, Koper MT, Hetterscheid DG. Challenges in reduction of dinitrogen by proton and electron transfer. *Chem Soc Rev* 2014;43:5183-91. DOI PubMed
  13. Shipman MA, Symes MD. Recent progress towards the electrosynthesis of ammonia from sustainable resources. *Catal Today* 2017;286:57-68. DOI
  14. Wang Q, Lei Y, Wang D, Li Y. Defect engineering in earth-abundant electrocatalysts for CO<sub>2</sub> and N<sub>2</sub> reduction. *Energy Environ Sci* 2019;12:1730-50. DOI
  15. Han S, Wei X, Huang Y, Zhang J, Yang J, Wang Z. Tuning the activity and selectivity of nitrogen reduction reaction on double-atom catalysts by B doping: a density functional theory study. *Nano Energy* 2022;99:107363. DOI
  16. Han J, Bao H, Wang J, et al. 3D N-doped ordered mesoporous carbon supported single-atom Fe-N-C catalysts with superior performance for oxygen reduction reaction and zinc-air battery. *Appl Catal B Environ* 2021;280:119411. DOI
  17. Yang L, Zhang X, Yu L, Hou J, Zhou Z, Lv R. Atomic Fe-N<sub>x</sub>/C in flexible carbon fiber membrane as binder-free air cathode for Zn-air batteries with stable cycling over 1000 h. *Adv Mater* 2022;34:2105410. DOI
  18. Chu C, Huang D, Gupta S, et al. Neighboring Pd single atoms surpass isolated single atoms for selective hydrodehalogenation catalysis. *Nat Commun* 2021;12:5179. DOI PubMed PMC
  19. Wu ZY, Karamad M, Yong X, et al. Electrochemical ammonia synthesis via nitrate reduction on Fe single atom catalyst. *Nat Commun* 2021;12:2870. DOI PubMed PMC
  20. Wu J, Zhou H, Li Q, et al. Densely populated isolated single Co-N site for efficient oxygen electrocatalysis. *Adv Energy Mater* 2019;9:1900149. DOI
  21. Rong X, Wang HJ, Lu XL, Si R, Lu TB. Controlled synthesis of a vacancy-defect single-atom catalyst for boosting CO<sub>2</sub> electroreduction. *Angew Chem Int Ed Engl* 2020;59:1961-5. DOI PubMed
  22. Yuan K, Lützenkirchen-Hecht D, Li L, et al. Boosting oxygen reduction of single iron active sites via geometric and electronic engineering: nitrogen and phosphorus dual coordination. *J Am Chem Soc* 2020;142:2404-12. DOI
  23. Wang Z, Jin X, Xu R, et al. Cooperation between dual metal atoms and nanoclusters enhances activity and stability for oxygen reduction and evolution. *ACS Nano* 2023;17:8622-33. DOI
  24. Tamtaji M, Cai S, Wu W, et al. Single and dual metal atom catalysts for enhanced singlet oxygen generation and oxygen reduction reaction. *J Mater Chem A* 2023;11:7513-25. DOI
  25. Chen W, Pei J, He CT, et al. Single tungsten atoms supported on MOF-derived N-doped carbon for robust electrochemical hydrogen evolution. *Adv Mater* 2018;30:1800396. DOI
  26. Wang X, Chen W, Zhang L, et al. Uncoordinated amine groups of metal-organic frameworks to anchor single Ru sites as chemoselective catalysts toward the hydrogenation of quinoline. *J Am Chem Soc* 2017;139:9419-22. DOI
  27. Zhang L, Fischer JMTA, Jia Y, et al. Coordination of atomic Co-Pt coupling species at carbon defects as active sites for oxygen reduction reaction. *J Am Chem Soc* 2018;140:10757-63. DOI
  28. Chen Z, Zhang X, Liu W, et al. Amination strategy to boost the CO<sub>2</sub> electroreduction current density of M-N/C single-atom catalysts to the industrial application level. *Energy Environ Sci* 2021;14:2349-56. DOI
  29. Guo W, Wang Z, Wang X, Wu Y. General design concept for single-atom catalysts toward heterogeneous catalysis. *Adv Mater* 2021;33:2004287. DOI
  30. Han X, Ling X, Wang Y, et al. Generation of nanoparticle, atomic-cluster, and single-atom cobalt catalysts from zeolitic imidazole frameworks by spatial isolation and their use in zinc-air batteries. *Angew Chem Int Ed Engl* 2019;58:5359-64. DOI
  31. Zhao C, Dai X, Yao T, et al. Ionic exchange of metal-organic frameworks to access single nickel sites for efficient electroreduction of CO<sub>2</sub>. *J Am Chem Soc* 2017;139:8078-81. DOI
  32. Jiao L, Zhu J, Zhang Y, et al. Non-bonding interaction of neighboring Fe and Ni single-atom pairs on MOF-derived N-doped carbon for enhanced CO<sub>2</sub> electroreduction. *J Am Chem Soc* 2021;143:19417-24. DOI
  33. Zhao Y, Zhou H, Chen W, et al. Two-step carbothermal welding to access atomically dispersed Pd<sub>1</sub> on three-dimensional zirconia nanonet for direct indole synthesis. *J Am Chem Soc* 2019;141:10590-4. DOI
  34. Ma X, Liu H, Yang W, Mao G, Zheng L, Jiang HL. Modulating coordination environment of single-atom catalysts and their proximity to photosensitive units for boosting MOF photocatalysis. *J Am Chem Soc* 2021;143:12220-9. DOI
  35. Fang X, Shang Q, Wang Y, et al. Single Pt atoms confined into a metal-organic framework for efficient photocatalysis. *Adv Mater* 2018;30:1705112. DOI
  36. Qiao B, Lin J, Wang A, Chen Y, Zhang T, Liu J. Highly active Au<sub>1</sub>/Co<sub>3</sub>O<sub>4</sub> single-atom catalyst for CO oxidation at room temperature. *Chinese J Catal* 2015;36:1505-11. DOI
  37. Peng W, Luo M, Xu X, et al. Spontaneous atomic ruthenium doping in Mo<sub>2</sub>CT<sub>x</sub> MXene defects enhances electrocatalytic activity for the nitrogen reduction reaction. *Adv Energy Mater* 2020;10:2001364. DOI
  38. Yang Y, Yang Q, Yang Y, et al. Enhancing water oxidation of Ru single atoms via oxygen-coordination bonding with NiFe layered double hydroxide. *ACS Catal* 2023;13:2771-9. DOI
  39. Xiang G, Zhao S, Wei C, et al. Atomically dispersed Au catalysts for preferential oxidation of CO in H<sub>2</sub>-rich stream. *Appl Catal B Environ* 2021;296:120385. DOI

40. Hannagan RT, Giannakakis G, Flytzani-Stephanopoulos M, Sykes ECH. Single-atom alloy catalysis. *Chem Rev* 2020;120:12044-88. DOI PubMed
41. Zhang T, Walsh AG, Yu J, Zhang P. Single-atom alloy catalysts: structural analysis, electronic properties and catalytic activities. *Chem Soc Rev* 2021;50:569-88. DOI
42. Xu Z, Ao Z, Yang M, Wang S. Recent progress in single-atom alloys: synthesis, properties, and applications in environmental catalysis. *J Hazard Mater* 2022;424:127427. DOI
43. Wang H, Jiao L, Zheng L, et al. PdBi single-atom alloy aerogels for efficient ethanol oxidation. *Adv Funct Mater* 2021;31:2103465. DOI
44. Shen X, Liu X, Wang S, et al. Synergistic modulation at atomically dispersed Fe/Au interface for selective CO<sub>2</sub> electroreduction. *Nano Lett* 2021;21:686-92. DOI
45. Mao J, He CT, Pei J, et al. Isolated Ni atoms dispersed on Ru nanosheets: high-performance electrocatalysts toward hydrogen oxidation reaction. *Nano Lett* 2020;20:3442-8. DOI
46. Wang Y, Cao L, Libretto NJ, et al. Ensemble effect in bimetallic electrocatalysts for CO<sub>2</sub> reduction. *J Am Chem Soc* 2019;141:16635-42. DOI
47. Chen C, Wu D, Li Z, et al. Ruthenium-based single-atom alloy with high electrocatalytic activity for hydrogen evolution. *Adv Energy Mater* 2019;9:1803913. DOI
48. Jiao J, Lin R, Liu S, et al. Copper atom-pair catalyst anchored on alloy nanowires for selective and efficient electrochemical reduction of CO<sub>2</sub>. *Nat Chem* 2019;11:222-8. DOI
49. Muravev V, Spezzati G, Su Y, et al. Interface dynamics of Pd-CeO<sub>2</sub> single-atom catalysts during CO oxidation. *Nat Catal* 2021;4:469-78. DOI
50. Zhang Z, Feng C, Liu C, et al. Electrochemical deposition as a universal route for fabricating single-atom catalysts. *Nat Commun* 2020;11:1215. DOI PubMed PMC
51. Zhang J, Liu J, Xi L, et al. Single-atom Au/NiFe layered double hydroxide electrocatalyst: probing the origin of activity for oxygen evolution reaction. *J Am Chem Soc* 2018;140:3876-9. DOI
52. Xu J, Li R, Xu C, et al. Underpotential-deposition synthesis and in-line electrochemical analysis of single-atom copper electrocatalysts. *Appl Catal B Environ* 2021;289:120028. DOI
53. Zhang J, Zhao Y, Guo X, et al. Single platinum atoms immobilized on an MXene as an efficient catalyst for the hydrogen evolution reaction. *Nat Catal* 2018;1:985-92. DOI
54. Jiang K, Liu B, Luo M, et al. Single platinum atoms embedded in nanoporous cobalt selenide as electrocatalyst for accelerating hydrogen evolution reaction. *Nat Commun* 2019;10:1743. DOI PubMed PMC
55. Zhang J, Pan Y, Feng D, et al. Mechanistic insight into the synergy between platinum single atom and cluster dual active sites boosting photocatalytic hydrogen evolution. *Adv Mater* 2023;35:e2300902. DOI
56. Yang Z, Chen C, Zhao Y, et al. Pt single atoms on CrN nanoparticles deliver outstanding activity and CO tolerance in the hydrogen oxidation reaction. *Adv Mater* 2023;35:e2208799. DOI
57. Li J, Banis MN, Ren Z, et al. Unveiling the nature of Pt single-atom catalyst during electrocatalytic hydrogen evolution and oxygen reduction reactions. *Small* 2021;17:2007245. DOI
58. Song Z, Wang Q, Li J, et al. Single-atom surface anchoring strategy via atomic layer deposition to achieve dual catalysts with remarkable electrochemical performance. *EcoMat* 2023;5:e12351. DOI
59. Zhang L, Wang Q, Li L, et al. Single atom surface engineering: a new strategy to boost electrochemical activities of Pt catalysts. *Nano Energy* 2022;93:106813. DOI
60. Jiao S, Kong M, Hu Z, Zhou S, Xu X, Liu L. Pt atom on the wall of atomic layer deposition (ALD)-made MoS<sub>2</sub> nanotubes for efficient hydrogen evolution. *Small* 2022;18:2105129. DOI
61. Yan H, Lin Y, Wu H, et al. Bottom-up precise synthesis of stable platinum dimers on graphene. *Nat Commun* 2017;8:1070. DOI PubMed PMC
62. Zafari M, Kumar D, Umer M, Kim KS. Machine learning-based high throughput screening for nitrogen fixation on boron-doped single atom catalysts. *J Mater Chem A* 2020;8:5209-16. DOI
63. Wang Z, Wang C, Hu Y, et al. Simultaneous diffusion of cation and anion to access N, S co-coordinated Bi-sites for enhanced CO<sub>2</sub> electroreduction. *Nano Res* 2021;14:2790-6. DOI
64. Shang H, Zhou X, Dong J, et al. Engineering unsymmetrically coordinated Cu-S<sub>1</sub>N<sub>3</sub> single atom sites with enhanced oxygen reduction activity. *Nat Commun* 2020;11:3049. DOI PubMed PMC
65. Li X, Yang X, Liu L, et al. Chemical vapor deposition for N/S-doped single Fe site catalysts for the oxygen reduction in direct methanol fuel cells. *ACS Catal* 2021;11:7450-9. DOI
66. Li Q, Chen W, Xiao H, et al. Fe isolated single atoms on S, N codoped carbon by copolymer pyrolysis strategy for highly efficient oxygen reduction reaction. *Adv Mater* 2018;30:e1800588. DOI
67. Zhang G, Tang F, Wang X, Wang L, Liu Y. Atomically dispersed Co-S-N active sites anchored on hierarchically porous carbon for efficient catalytic hydrogenation of nitro compounds. *ACS Catal* 2022;12:5786-94. DOI
68. Wang M, Yang W, Li X, et al. Atomically dispersed Fe-heteroatom (N, S) bridge sites anchored on carbon nanosheets for promoting oxygen reduction reaction. *ACS Energy Lett* 2021;6:379-86. DOI
69. Zhang H, Liu Y, Chen T, Zhang J, Zhang J, Lou XWD. Unveiling the activity origin of electrocatalytic oxygen evolution over

- isolated Ni atoms supported on a N-doped carbon matrix. *Adv Mater* 2019;31:1904548. DOI
70. Jiang R, Li L, Sheng T, Hu G, Chen Y, Wang L. Edge-site engineering of atomically dispersed Fe-N<sub>4</sub> by selective C-N bond cleavage for enhanced oxygen reduction reaction activities. *J Am Chem Soc* 2018;140:11594-8. DOI
71. Cai Y, Fu J, Zhou Y, et al. Insights on forming N,O-coordinated Cu single-atom catalysts for electrochemical reduction CO<sub>2</sub> to methane. *Nat Commun* 2021;12:586. DOI PubMed PMC
72. Wang F, Zhang R, Zhang Y, et al. Modulating electronic structure of atomically dispersed nickel sites through boron and nitrogen dual coordination boosts oxygen reduction. *Adv Funct Mater* 2023;33:2213863. DOI
73. Jiao D, Liu Y, Cai Q, Zhao J. Coordination tunes the activity and selectivity of the nitrogen reduction reaction on single-atom iron catalysts: a computational study. *J Mater Chem A* 2021;9:1240-51. DOI
74. Liu W, Zhang L, Liu X, et al. Discriminating catalytically active FeN<sub>x</sub> species of atomically dispersed Fe-N-C catalyst for selective oxidation of the C-H bond. *J Am Chem Soc* 2017;139:10790-8. DOI
75. Zhang Y, Jiao L, Yang W, Xie C, Jiang HL. Rational fabrication of low-coordinate single-atom Ni electrocatalysts by MOFs for highly selective CO<sub>2</sub> reduction. *Angew Chem Int Ed Engl* 2021;60:7607-11. DOI
76. Wang J, Qiu W, Li G, et al. Coordinatively deficient single-atom Fe-N-C electrocatalyst with optimized electronic structure for high-performance lithium-sulfur batteries. *Energy Storage Mater* 2022;46:269-77. DOI
77. Zhang S, Ao X, Huang J, et al. Isolated single-atom Ni-N<sub>5</sub> catalytic site in hollow porous carbon capsules for efficient lithium-sulfur batteries. *Nano Lett* 2021;21:9691-8. DOI
78. Fan B, Wang H, Han X, Deng Y, Hu W. Single atoms (Pt, Ir and Rh) anchored on activated NiCo LDH for alkaline hydrogen evolution reaction. *Chem Commun* 2022;58:8254-7. DOI
79. Li X, Shen P, Luo Y, et al. PdFe single-atom alloy metallene for N<sub>2</sub> electroreduction. *Angew Chem Int Ed Engl* 2022;61:e202205923. DOI
80. Pan J, Zhang G, Guan Z, et al. Anchoring Ni single atoms on sulfur-vacancy-enriched ZnIn<sub>2</sub>S<sub>4</sub> nanosheets for boosting photocatalytic hydrogen evolution. *J Energy Chem* 2021;58:408-14. DOI
81. Han Z, Zhao S, Xiao J, et al. Engineering *d-p* orbital hybridization in single-atom metal-embedded three-dimensional electrodes for Li-S batteries. *Adv Mater* 2021;33:2105947. DOI
82. Han B, Guo Y, Huang Y, et al. Strong metal-support interactions between Pt single atoms and TiO<sub>2</sub>. *Angew Chem Int Ed Engl* 2020;59:11824-9. DOI
83. Hu B, Sun K, Zhuang Z, et al. Distinct crystal-facet-dependent behaviors for single-atom palladium-on-ceria catalysts: enhanced stabilization and catalytic properties. *Adv Mater* 2022;34:2107721. DOI
84. Shi Y, Ma ZR, Xiao YY, et al. Electronic metal-support interaction modulates single-atom platinum catalysis for hydrogen evolution reaction. *Nat Commun* 2021;12:3021. DOI PubMed PMC
85. Qu Y, Wang L, Li Z, et al. ambient synthesis of single-atom catalysts from bulk metal via trapping of atoms by surface dangling bonds. *Adv Mater* 2019;31:1904496. DOI
86. Hu X, Luo G, Zhao Q, et al. Ru single atoms on N-doped carbon by spatial confinement and ionic substitution strategies for high-performance Li-O<sub>2</sub> batteries. *J Am Chem Soc* 2020;142:16776-86. DOI
87. Liu L, Wang N, Zhu C, et al. Direct imaging of atomically dispersed molybdenum that enables location of aluminum in the framework of zeolite ZSM-5. *Angew Chem Int Ed Engl* 2020;59:819-25. DOI
88. Chen S, Li WH, Jiang W, et al. MOF encapsulating N-heterocyclic carbene-ligated copper single-atom site catalyst towards efficient methane electrosynthesis. *Angew Chem Int Ed Engl* 2022;61:e202114450. DOI
89. Liu G, Huang Y, Lv H, et al. Confining single-atom Pd on g-C<sub>3</sub>N<sub>4</sub> with carbon vacancies towards enhanced photocatalytic NO conversion. *Appl Catal B Environ* 2021;284:119683. DOI
90. Su L, Wang P, Ma X, Wang J, Zhan S. Regulating local electron density of iron single sites by introducing nitrogen vacancies for efficient photo-fenton process. *Angew Chem Int Ed Engl* 2021;60:21261-6. DOI PubMed
91. Kumar A, Liu X, Lee J, et al. Discovering ultrahigh loading of single-metal-atoms *via* surface tensile-strain for unprecedented urea electrolysis. *Energy Environ Sci* 2021;14:6494-505. DOI
92. Chen W, Pei J, He CT, et al. Rational design of single molybdenum atoms anchored on N-doped carbon for effective hydrogen evolution reaction. *Angew Chem Int Ed Engl* 2017;56:16086-90. DOI
93. Shah K, Dai R, Mateen M, et al. Cobalt single atom incorporated in ruthenium oxide sphere: a robust bifunctional electrocatalyst for HER and OER. *Angew Chem Int Ed Engl* 2022;61:e202114951. DOI
94. Yang Y, Qian Y, Li H, et al. O-coordinated W-Mo dual-atom catalyst for pH-universal electrocatalytic hydrogen evolution. *Sci Adv* 2020;6:eaba6586. DOI PubMed PMC
95. Cai C, Wang M, Han S, et al. Ultrahigh oxygen evolution reaction activity achieved using Ir single atoms on amorphous CoO<sub>x</sub> nanosheets. *ACS Catal* 2021;11:123-30. DOI
96. Wang Q, Huang X, Zhao ZL, et al. Ultrahigh-loading of Ir single atoms on NiO matrix to dramatically enhance oxygen evolution reaction. *J Am Chem Soc* 2020;142:7425-33. DOI
97. Zhou X, Gao J, Hu Y, et al. Theoretically revealed and experimentally demonstrated synergistic electronic interaction of CoFe dual-metal sites on N-doped carbon for boosting both oxygen reduction and evolution reactions. *Nano Lett* 2022;22:3392-9. DOI
98. Wang Z, Jin X, Zhu C, et al. Atomically dispersed Co<sub>2</sub>-N<sub>6</sub> and Fe-N<sub>4</sub> costructures boost oxygen reduction reaction in both alkaline and acidic media. *Adv Mater* 2021;33:2104718. DOI

99. Zhang Z, Sun J, Wang F, Dai L. Efficient oxygen reduction reaction (ORR) catalysts based on single iron atoms dispersed on a hierarchically structured porous carbon framework. *Angew Chem Int Ed Engl* 2018;57:9038-43. DOI PubMed
100. Bai X, Zhao Z, Lu G. Breaking the scaling relationship on single-atom embedded MBene for selective CO<sub>2</sub> electroreduction. *J Phys Chem Lett* 2023;14:5172-80. DOI PubMed
101. Xiao J, Liu Z, Wang X, Li F, Zhao Z. Homonuclear multi-atom catalysts for CO<sub>2</sub> electroreduction: a comparison density functional theory study with their single-atom counterparts. *J Mater Chem A* 2023;11:25662-70. DOI
102. Chen Z, Chen LX, Yang CC, Jiang Q. Atomic (single, double, and triple atoms) catalysis: frontiers, opportunities, and challenges. *J Mater Chem A* 2019;7:3492-515. DOI
103. Zhao D, Zhuang Z, Cao X, et al. Atomic site electrocatalysts for water splitting, oxygen reduction and selective oxidation. *Chem Soc Rev* 2020;49:2215-64. DOI
104. Yang Y, Yang Y, Pei Z, et al. Recent progress of carbon-supported single-atom catalysts for energy conversion and storage. *Matter* 2020;3:1442-76. DOI
105. Li P, Jin Z, Fang Z, Yu G. A single-site iron catalyst with preoccupied active centers that achieves selective ammonia electrosynthesis from nitrate. *Energy Environ Sci* 2021;14:3522-31. DOI
106. Lv X, Wei W, Li F, Huang B, Dai Y. Metal-free B@g-CN: visible/infrared light-driven single atom photocatalyst enables spontaneous dinitrogen reduction to ammonia. *Nano Lett* 2019;19:6391-9. DOI
107. Chen Y, Zhang X, Qin J, Liu R. High-throughput screening of single metal atom anchored on N-doped boron phosphide for N<sub>2</sub> reduction. *Nanoscale* 2021;13:13437-50. DOI
108. Choi C, Back S, Kim NY, Lim J, Kim YH, Jung Y. Suppression of hydrogen evolution reaction in electrochemical N<sub>2</sub> reduction using single-atom catalysts: a computational guideline. *ACS Catal* 2018;8:7517-25. DOI
109. Zhao J, Chen Z. Single Mo atom supported on defective boron nitride monolayer as an efficient electrocatalyst for nitrogen fixation: a computational study. *J Am Chem Soc* 2017;139:12480-7. DOI
110. Liu H, Han S, Zhao Y, et al. Surfactant-free atomically ultrathin rhodium nanosheet nanoassemblies for efficient nitrogen electroreduction. *J Mater Chem A* 2018;6:3211-7. DOI
111. Shi MM, Bao D, Wulan BR, et al. Au sub-nanoclusters on TiO<sub>2</sub> toward highly efficient and selective electrocatalyst for N<sub>2</sub> conversion to NH<sub>3</sub> at ambient conditions. *Adv Mater* 2017;29:1606550. DOI
112. Tao H, Choi C, Ding L, et al. Nitrogen fixation by Ru single-atom electrocatalytic reduction. *Chem* 2019;5:204-14. DOI
113. Chen K, Ma Z, Li X, Kang J, Ma D, Chu K. Single-atom Bi alloyed Pd metallene for nitrate electroreduction to ammonia. *Adv Funct Mater* 2023;33:2209890. DOI
114. Wang X, Wang W, Qiao M, et al. Atomically dispersed Au<sub>1</sub> catalyst towards efficient electrochemical synthesis of ammonia. *Sci Bull* 2018;63:1246-53. DOI
115. Sun H, Yin H, Shi W, et al. Porous β-FeOOH nanotube stabilizing Au single atom for high-efficiency nitrogen fixation. *Nano Res* 2022;15:3026-33. DOI
116. Geng Z, Liu Y, Kong X, et al. Achieving a record-high yield rate of 120.9 μg<sub>NH<sub>3</sub></sub> mg<sub>cat.</sub><sup>-1</sup> h<sup>-1</sup> for N<sub>2</sub> electrochemical reduction over Ru single-atom catalysts. *Adv Mater* 2018;30:1803498. DOI
117. He T, Puente Santiago AR, Du A. Atomically embedded asymmetrical dual-metal dimers on N-doped graphene for ultra-efficient nitrogen reduction reaction. *J Catal* 2020;388:77-83. DOI
118. Han L, Ren Z, Ou P, et al. Modulating single-atom palladium sites with copper for enhanced ambient ammonia electrosynthesis. *Angew Chem Int Ed Engl* 2021;60:345-50. DOI
119. Shang S, Xiong W, Yang C, et al. Atomically dispersed iron metal site in a porphyrin-based metal-organic framework for photocatalytic nitrogen fixation. *ACS Nano* 2021;15:9670-8. DOI
120. Li Y, Li J, Huang J, et al. Boosting electroreduction kinetics of nitrogen to ammonia via tuning electron distribution of single-atomic iron sites. *Angew Chem Int Ed Engl* 2021;60:9078-85. DOI
121. Hu R, Yu Y, Li Y, et al. Rational design of bimetallic atoms supported on C<sub>3</sub>N monolayer to break the linear relations for efficient electrochemical nitrogen reduction. *Nano Res* 2022;15:8656-64. DOI
122. Li XF, Li QK, Cheng J, et al. Conversion of dinitrogen to ammonia by FeN<sub>3</sub>-embedded graphene. *J Am Chem Soc* 2016;138:8706-9. DOI
123. Zhang R, Jiao L, Yang W, Wan G, Jiang H. Single-atom catalysts templated by metal-organic frameworks for electrochemical nitrogen reduction. *J Mater Chem A* 2019;7:26371-7. DOI
124. Liu K, Fu J, Zhu L, et al. Single-atom transition metals supported on black phosphorene for electrochemical nitrogen reduction. *Nanoscale* 2020;12:4903-8. DOI
125. Lü F, Zhao S, Guo R, et al. Nitrogen-coordinated single Fe sites for efficient electrocatalytic N<sub>2</sub> fixation in neutral media. *Nano Energy* 2019;61:420-7. DOI
126. Wang M, Liu S, Qian T, et al. Over 56.55% Faradaic efficiency of ambient ammonia synthesis enabled by positively shifting the reaction potential. *Nat Commun* 2019;10:341. DOI PubMed PMC
127. Zhang S, Jin M, Shi T, et al. Electrocatalytically active Fe-(O-C<sub>2</sub>)<sub>4</sub> single-atom sites for efficient reduction of nitrogen to ammonia. *Angew Chem Int Ed Engl* 2020;59:13423-9. DOI
128. Zhang L, Zhao W, Zhang W, Chen J, Hu Z. gt-C<sub>3</sub>N<sub>4</sub> coordinated single atom as an efficient electrocatalyst for nitrogen reduction reaction. *Nano Res* 2019;12:1181-6. DOI

129. Lin L, Wei F, Jiang R, Huang Y, Lin S. The role of central heteroatom in electrochemical nitrogen reduction catalyzed by polyoxometalate-supported single-atom catalyst. *Nano Res* 2023;16:309-17. DOI
130. Sahoo SK, Heske J, Antonietti M, Qin Q, Oschatz M, Kühne TD. Electrochemical N<sub>2</sub> reduction to ammonia using single Au/Fe atoms supported on nitrogen-doped porous carbon. *ACS Appl Energy Mater* 2020;3:10061-9. DOI PubMed PMC
131. Li J, Chen S, Quan F, et al. Accelerated dinitrogen electroreduction to ammonia via interfacial polarization triggered by single-atom protrusions. *Chem* 2020;6:885-901. DOI
132. Su H, Chen L, Chen Y, et al. Single atoms of iron on MoS<sub>2</sub> nanosheets for N<sub>2</sub> electroreduction into ammonia. *Angew Chem Int Ed Engl* 2020;59:20411-6. DOI
133. Ling C, Bai X, Ouyang Y, Du A, Wang J. Single molybdenum atom anchored on N-doped carbon as a promising electrocatalyst for nitrogen reduction into ammonia at ambient conditions. *J Phys Chem C* 2018;122:16842-7. DOI
134. Han L, Liu X, Chen J, et al. Atomically dispersed molybdenum catalysts for efficient ambient nitrogen fixation. *Angew Chem Int Ed Engl* 2019;58:2321-5. DOI
135. Fan B, Wang H, Zhang H, et al. Phase transfer of Mo<sub>2</sub>C induced by boron doping to boost nitrogen reduction reaction catalytic activity. *Adv Funct Mater* 2022;32:2110783. DOI
136. Song Y, Wang H, Song Z, et al. Ni-doped Mo<sub>2</sub>C anchored on graphitized porous carbon for boosting electrocatalytic N<sub>2</sub> reduction. *ACS Appl Mater Interfaces* 2022;14:17273-81. DOI
137. Ma Y, Yang T, Zou H, et al. Synergizing Mo single atoms and Mo<sub>2</sub>C nanoparticles on CNTs synchronizes selectivity and activity of electrocatalytic N<sub>2</sub> reduction to ammonia. *Adv Mater* 2020;32:2002177. DOI
138. Wang J, Zhang Z, Qi S, et al. Photo-assisted high performance single atom electrocatalysis of the N<sub>2</sub> reduction reaction by a Mo-embedded covalent organic framework. *J Mater Chem A* 2021;9:19949-57. DOI
139. Chen L, He C, Wang R, et al. Potential active sites of Mo single atoms for electrocatalytic reduction of N<sub>2</sub>. *Chinese Chem Lett* 2021;32:53-6. DOI
140. Shi L, Bi S, Qi Y, et al. Anchoring Mo single-atom sites on B/N codoped porous carbon nanotubes for electrochemical reduction of N<sub>2</sub> to NH<sub>3</sub>. *ACS Catal* 2022;12:7655-63. DOI
141. Zhang C, Wang Z, Lei J, Ma L, Yakobson BI, Tour JM. Atomic molybdenum for synthesis of ammonia with 50% Faradic efficiency. *Small* 2022;18:e2106327. DOI
142. Mukherjee S, Yang X, Shan W, et al. Atomically dispersed single Ni site catalysts for nitrogen reduction toward electrochemical ammonia synthesis using N<sub>2</sub> and H<sub>2</sub>O. *Small Methods* 2020;4:1900821. DOI
143. Han L, Hou M, Ou P, et al. Local modulation of single-atomic Mn sites for enhanced ambient ammonia electrosynthesis. *ACS Catal* 2021;11:509-16. DOI
144. Zang W, Yang T, Zou H, et al. Copper single atoms anchored in porous nitrogen-doped carbon as efficient pH-universal catalysts for the nitrogen reduction reaction. *ACS Catal* 2019;9:10166-73. DOI
145. Zhang W, Fu Y, Peng Q, et al. Supramolecular preorganization effect to access single cobalt sites for enhanced photocatalytic hydrogen evolution and nitrogen fixation. *Chem Eng J* 2020;394:124822. DOI
146. Liu J, Kong X, Zheng L, Guo X, Liu X, Shui J. Rare earth single-atom catalysts for nitrogen and carbon dioxide reduction. *ACS Nano* 2020;14:1093-101. DOI